

Finite-temperature, Anharmonicity, and Duschinsky Effects on the Two-dimensional Electronic Spectra from Ab Initio Thermo-field Gaussian Wavepacket Dynamics

Tomislav Begušić* and Jiří Vaníček*

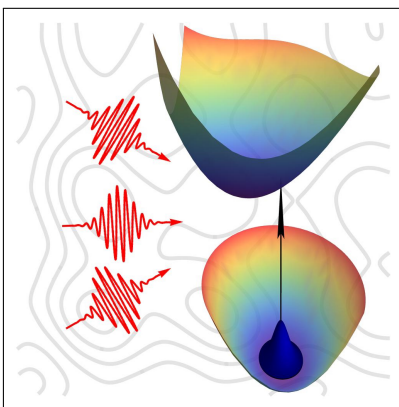
*Laboratory of Theoretical Physical Chemistry, Institut des Sciences et Ingénierie Chimiques,
Ecole Polytechnique Fédérale de Lausanne (EPFL), CH-1015, Lausanne, Switzerland*

E-mail: tomlav.begusic@epfl.ch; jiri.vanicek@epfl.ch

Abstract

Accurate description of finite-temperature vibrational dynamics is indispensable in the computation of two-dimensional electronic spectra. Such simulations are often based on the density matrix evolution, statistical averaging of initial vibrational states, or approximate classical or semiclassical limits. While many practical approaches exist, they are often of limited accuracy and difficult to interpret. Here, we use the concept of thermo-field dynamics to derive an exact finite-temperature expression that lends itself to an intuitive wavepacket-based interpretation. Furthermore, an efficient method for computing finite-temperature two-dimensional spectra is obtained by combining the exact thermo-field dynamics approach with the thawed Gaussian approximation for the wavepacket dynamics, which is exact for any displaced, distorted, and Duschinsky-rotated harmonic potential but also accounts partially for anharmonicity effects in general potentials. Using this new method, we directly relate a symmetry breaking of the two-dimensional signal to the deviation from the conventional Brownian oscillator picture.

Graphical TOC Entry



Multidimensional optical spectroscopy is an emerging experimental method for studying molecular photochemistry and photophysics, but its further development and the interpretation of new experiments rely heavily on theoretical modeling.¹⁻⁷ To this end, a number of theoretical methods⁸⁻¹⁵ were developed to account for typical vibrational-electronic effects occurring in molecular systems, such as anharmonicity, different curvatures of the ground- and excited-state potential energy surfaces, or mode-mode mixing (Duschinsky rotation).¹⁶⁻²⁰ In its original formulation, the second-order cumulant expansion²¹⁻²⁴ is exact only for the Brownian oscillator (i.e., displaced harmonic) model and cannot treat the intermode coupling in the excited state. Although this basic molecular model shaped our understanding of steady-state, ultrafast, and multidimensional electronic spectroscopy in the past decades, it is inadequate for many molecules that exhibit Duschinsky and anharmonicity effects.^{12,14} Similar limitations are met when using the semiclassical phase averaging,^{22,25} also known as the Wigner-averaged classical limit²⁶⁻³⁰ or dephasing representation.³¹⁻³⁴ The recently developed third-order cumulant approach seems to overcome these limitations,^{10,13,14} yet it is accurate only in systems with weakly coupled or distorted modes.¹⁴

In contrast, quantum dynamics methods³⁵⁻⁴⁰ are well suited for describing the evolution of nuclear wavepackets but often neglect temperature effects. To avoid the impractical Boltzmann averaging over the initial states, a number of alternative strategies for including temperature in wavepacket-based methods have been proposed.⁴¹⁻⁴⁷ We turn to the so-called thermo-field dynamics,^{48,49} which transforms the von Neumann evolution of a density matrix to a Schrödinger equation with a doubled number of degrees of freedom. This approach has only recently been introduced in chemistry for solving the electronic structure,⁵⁰⁻⁵² vibronic,⁵³⁻⁵⁶ and spectroscopic⁵⁷ problems at finite temperature. Here, we show how it could be used to compute two-dimensional vibronic spectra. The finite-temperature treatment is combined with the thawed Gaussian approximation,⁵⁸ an efficient first-principles^{59,60} method for wavepacket propagation, and applied to the stimulated emission and ground-state bleach signals of azulene.

In two-dimensional spectroscopy, a nonlinear time-dependent polarization^{22,61}

$$P^{(3)}(t, t_2, t_1) = \left(\frac{i}{\hbar}\right)^3 \int_0^\infty dt''' \int_0^\infty dt'' \int_0^\infty dt' R^{(3)}(t''', t'', t') E_{t_1, t_2}(t-t''') E_{t_1, t_2}(t-t''-t''') E_{t_1, t_2}(t-t'-t''-t''') \quad (1)$$

is induced in the sample through interaction with the electric field $E_{t_1, t_2}(t)$ comprised of three light pulses centered at times $-t_2 - t_1$, $-t_2$, and 0, where t_1 is the delay between the first two pulses, t_2 is the delay between the second and third pulses, and $R^{(3)}(t''', t'', t')$ is the third-order response function.²² In a heterodyne detection scheme, the measured signal is⁶¹

$$S(t_3, t_2, t_1) \propto i \int_{-\infty}^{\infty} E_{\text{LO}}(t) P^{(3)}(t, t_2, t_1) dt, \quad (2)$$

where $E_{\text{LO}}(t)$ is the fourth, local oscillator pulse centered at time t_3 after the third pulse. The two-dimensional spectrum is obtained by scanning $S(t_3, t_2, t_1)$ as a function of the three time delays and Fourier transforming over t_1 and t_3 . We focus on the absorptive two-dimensional spectrum^{62,63}

$$\tilde{S}(\omega_3, t_2, \omega_1) = \tilde{S}_{\text{R}}(\omega_3, t_2, \omega_1) + \tilde{S}_{\text{NR}}(\omega_3, t_2, \omega_1), \quad (3)$$

and assume ultrashort and nonoverlapping pulse approximations, where the rephasing and nonrephasing spectra,⁶¹

$$\tilde{S}_{\text{R}}(\omega_3, t_2, \omega_1) = \text{Re} \int_0^\infty dt_3 e^{i\omega_3 t_3} \int_0^\infty dt_1 e^{-i\omega_1 t_1} S_{\text{R}}(t_3, t_2, t_1), \quad (4)$$

$$\tilde{S}_{\text{NR}}(\omega_3, t_2, \omega_1) = \text{Re} \int_0^\infty dt_3 e^{i\omega_3 t_3} \int_0^\infty dt_1 e^{i\omega_1 t_1} S_{\text{NR}}(t_3, t_2, t_1), \quad (5)$$

are defined through

$$S_{\text{R}}(t_3, t_2, t_1) = C_1(t_1 + t_2, t_3, t_2 + t_3) + C_1(t_1, t_2 + t_3, t_3) - C_3(t_2, t_3, t_1 + t_2 + t_3)^*, \quad (6)$$

$$S_{\text{NR}}(t_3, t_2, t_1) = C_1(t_2, t_3, t_1 + t_2 + t_3) + C_1(-t_3, -t_2, t_1) - C_3(t_1 + t_2, t_3, t_2 + t_3)^*, \quad (7)$$

and

$$C_i(\tau_a, \tau_b, \tau_c) = \text{Tr}[\hat{\rho}\hat{\mu}_{12}e^{i\hat{H}_2\tau_a/\hbar}\hat{\mu}_{2i}e^{i\hat{H}_i\tau_b/\hbar}\hat{\mu}_{i2}e^{-i\hat{H}_2\tau_c/\hbar}\hat{\mu}_{21}e^{-i\hat{H}_1(\tau_a+\tau_b-\tau_c)/\hbar}], \quad i = 1, 3. \quad (8)$$

In Eq. (8), \hat{H}_j are the vibrational Hamiltonians corresponding to the ground ($j = 1$) and excited ($j = 2, 3$) electronic states, $\hat{\rho} = \exp(-\beta\hat{H}_1)/\text{Tr}[\exp(-\beta\hat{H}_1)]$ is the vibrational density operator at temperature $T = 1/k_B\beta$, and $\hat{\mu}_{ij} = \hat{\mu}_{ij} \cdot \vec{e}$ is the electronic transition dipole moment between electronic states i and j projected on the polarization unit vector \vec{e} of the external electric field. Correlation function C_1 corresponds to the stimulated emission and ground-state bleach processes, while C_3 , which involves a higher excited electronic state, corresponds to the excited-state absorption (see Sec. 1 of the Supporting Information). Although the excited-state absorption term involves, in general, a sum over several higher excited states ($i \geq 3$), here, for the sake of brevity, we consider only one such state.

An intuitive physical interpretation of Eq. (8) is available in the zero-temperature limit, where the density operator $\hat{\rho} = |1, g\rangle\langle 1, g|$ is given in terms of the ground vibrational state $|1, g\rangle$ of the ground electronic state. Then,⁴⁰

$$C_i(\tau_a, \tau_b, \tau_c) = \langle \phi_{\tau_b, \tau_a}^{(i)} | \phi_{0, \tau_c}^{(i)} \rangle, \quad (9)$$

where

$$|\phi_{\tau, t}^{(i)}\rangle = e^{-i\hat{H}'_i\tau/\hbar}\hat{\mu}_{i2}e^{-i\hat{H}'_2t/\hbar}\hat{\mu}_{21}|1, g\rangle, \quad (10)$$

$\hat{H}'_i = \hat{H}_i - \hbar\omega_{1,g}$, and $\hbar\omega_{1,g} = \langle 1, g | \hat{H}_1 | 1, g \rangle$. In Fig. 1, we illustrate how Eq. (9) is evaluated for stimulated emission contribution $C_1(t_1 + t_2, t_3, t_2 + t_3)$ [Eq. (8)] to the rephasing signal [Eq. (6)]. The bra nuclear wavepacket is first evolved for a time $\tau_a = t_1 + t_2$ in the excited electronic state and then for a time $\tau_b = t_3$ in the ground state; the ket wavepacket is in the ground electronic state during t_1 and evolves in the excited state for a time $\tau_c = t_2 + t_3$. In general, during time delays t_1 and t_3 , also known as coherence and detection times, the

bra and ket wavepackets evolve on different potential energy surfaces; during the so-called population time t_2 , the two wavepackets are in the same electronic state: in the ground state for the ground-state bleach contribution and in the excited electronic state for the stimulated emission and excited-state absorption components.

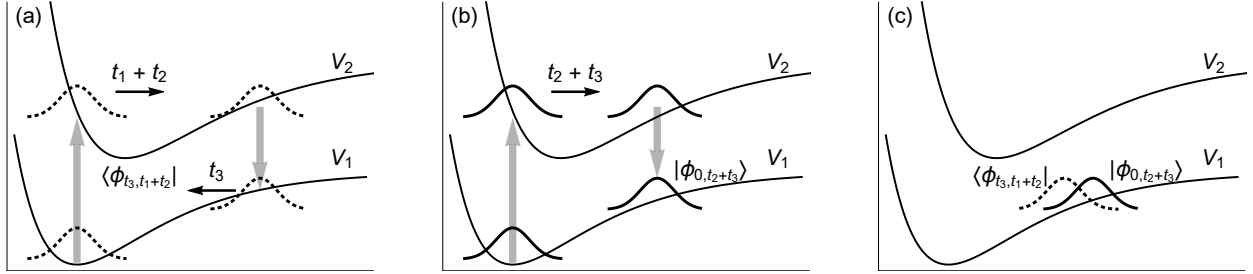


Figure 1: Evolution of the bra (a, dotted line) and ket (b, solid line) wavepackets of Eq. (9) for $\tau_a = t_1 + t_2$, $\tau_b = t_3$, and $\tau_c = t_2 + t_3$. Their overlap (c) is stimulated emission term $C_1(t_1 + t_2, t_3, t_2 + t_3)$ [Eq. (8)] of rephasing signal $S_R(t_3, t_2, t_1)$ [Eq. (6)].

We now address the question of whether it is possible to retain the simple wavepacket picture without neglecting finite-temperature effects. To answer this question in the affirmative, we employ thermo-field dynamics, which maps the evolution of a density operator at finite temperature to the evolution of a wavefunction with a doubled number of coordinates. In the thermo-field dynamics theory,⁴⁸ the thermal vacuum is defined as

$$|\bar{0}(\beta)\rangle = \hat{\rho}^{1/2} \sum_k |k\tilde{k}\rangle, \quad (11)$$

where $|k\tilde{k}\rangle = |k\rangle|\tilde{k}\rangle$ is the basis vector of the tensor-product space obtained from the physical (with basis $\{|k\rangle\}$) and “fictitious” (with basis $\{|\tilde{k}\rangle\}$) Hilbert spaces. We note that physical operators (denoted only by hat $\hat{\cdot}$, such as $\hat{\rho}$ or $\hat{\mu}$) act only on the physical subspace. With these definitions, Eq. (8) can be rewritten as

$$C_i(\tau_a, \tau_b, \tau_c) = \langle \bar{\phi}_{\tau_b, \tau_a}^{(i)} | \bar{\phi}_{0, \tau_c}^{(i)} \rangle, \quad (12)$$

where

$$|\bar{\phi}_{\tau,t}^{(i)}\rangle = e^{-i\hat{H}_i\tau/\hbar}\hat{\mu}_{i2}e^{-i\hat{H}_2t/\hbar}\hat{\mu}_{21}|\bar{0}(\beta)\rangle \quad (13)$$

is the analogue of $|\phi_{\tau,t}^{(i)}\rangle$ from Eq. (10),

$$\hat{H}_j = \hat{H}_j - \hat{H}_1 \quad (j = 1, 2, 3) \quad (14)$$

is the Hamiltonian acting in the full, tensor-product space, and \hat{H}_1 is the ground-state vibrational Hamiltonian acting in the fictitious space only. The proof of Eq. (12) goes as follows:

$$C_i(\tau_a, \tau_b, \tau_c) = \langle \bar{0}(\beta) | \hat{\mu}_{12} e^{i\hat{H}_2\tau_a/\hbar} \hat{\mu}_{2i} e^{i\hat{H}_i\tau_b/\hbar} \hat{\mu}_{i2} e^{-i\hat{H}_2\tau_c/\hbar} \hat{\mu}_{21} | \bar{0}(\beta) \rangle \quad (15)$$

$$= \sum_{k_1, k_2} \langle k_1 \tilde{k}_1 | \hat{\rho}^{1/2} \hat{\mu}_{12} e^{i(\hat{H}_2 - \hat{H}_1)\tau_a/\hbar} \hat{\mu}_{2i} e^{i(\hat{H}_i - \hat{H}_1)\tau_b/\hbar} \hat{\mu}_{i2} e^{-i(\hat{H}_2 - \hat{H}_1)\tau_c/\hbar} \hat{\mu}_{21} \hat{\rho}^{1/2} | k_2 \tilde{k}_2 \rangle \quad (16)$$

$$= \sum_{k_1, k_2} \langle k_1 | \hat{\rho}^{1/2} \hat{\mu}_{12} e^{i\hat{H}_2\tau_a/\hbar} \hat{\mu}_{2i} e^{i\hat{H}_i\tau_b/\hbar} \hat{\mu}_{i2} e^{-i\hat{H}_2\tau_c/\hbar} \hat{\mu}_{21} \hat{\rho}^{1/2} | k_2 \rangle \langle \tilde{k}_1 | e^{-i\hat{H}_1(\tau_a + \tau_b - \tau_c)/\hbar} | \tilde{k}_2 \rangle \quad (17)$$

$$= \sum_{k_1, k_2} \langle k_1 | \hat{\rho}^{1/2} \hat{\mu}_{12} e^{i\hat{H}_2\tau_a/\hbar} \hat{\mu}_{2i} e^{i\hat{H}_i\tau_b/\hbar} \hat{\mu}_{i2} e^{-i\hat{H}_2\tau_c/\hbar} \hat{\mu}_{21} \hat{\rho}^{1/2} | k_2 \rangle \langle k_2 | e^{-i\hat{H}_1(\tau_a + \tau_b - \tau_c)/\hbar} | k_1 \rangle \quad (18)$$

$$= \sum_{k_1} \langle k_1 | \hat{\rho}^{1/2} \hat{\mu}_{12} e^{i\hat{H}_2\tau_a/\hbar} \hat{\mu}_{2i} e^{i\hat{H}_i\tau_b/\hbar} \hat{\mu}_{i2} e^{-i\hat{H}_2\tau_c/\hbar} \hat{\mu}_{21} e^{-i\hat{H}_1(\tau_a + \tau_b - \tau_c)/\hbar} \hat{\rho}^{1/2} | k_1 \rangle \quad (19)$$

$$= \text{Tr}[\hat{\rho} \hat{\mu}_{12} e^{i\hat{H}_2\tau_a/\hbar} \hat{\mu}_{2i} e^{i\hat{H}_i\tau_b/\hbar} \hat{\mu}_{i2} e^{-i\hat{H}_2\tau_c/\hbar} \hat{\mu}_{21} e^{-i\hat{H}_1(\tau_a + \tau_b - \tau_c)/\hbar}]. \quad (20)$$

Equation (15) is obtained from Eq. (12) by inserting the definition (13) of $\bar{\phi}_{\tau,t}^{(i)}$, while Eq. (16) results upon substituting relation (11) for $|\bar{0}(\beta)\rangle$; in going from Eq. (16) to (17) we used the fact that operators acting in different subspaces commute. In going from (17) to (18) we used the conjugation rules relating the physical and fictitious spaces (see Sec. 2 of the Supporting Information). The resolution of identity and commutation of $\hat{\rho}^{1/2}$ with \hat{H}_1 were used to obtain Eq. (19), and the definition and cyclic property of the trace to obtain Eq. (20).

Remarkably, the result (12) has exactly the same form as the zero-temperature expression (9) and can be interpreted as in Fig. 1. It also allows finite-temperature effects to be

included in regular wavefunction-based codes, by modifying only the definition of the initial state and the Hamiltonians under which this state is evolved. In Sec. 3 of the Supporting Information, we prove that the same wavepacket picture can be justified even beyond the Born–Oppenheimer approximation, which was invoked implicitly in Eqs. (6)–(8). To avoid exponentially scaling exact quantum methods on precomputed potential energy surfaces^{64–67} or computationally demanding multiple-trajectory^{68–82} approaches, we propose using the simple, yet efficient, single-trajectory thawed Gaussian approximation, which can be interfaced with on-the-fly ab initio evaluation of potential energy information.⁸³

Let us consider a Gaussian wavepacket

$$\psi_t(q) = e^{\frac{i}{\hbar}[(q-q_t)^T \cdot A_t \cdot (q-q_t) + p_t^T \cdot (q-q_t) + \gamma_t]}, \quad (21)$$

where q_t and p_t are the real, D -dimensional expectation values of position and momentum, respectively, A_t is a $D \times D$ complex symmetric matrix with positive-definite imaginary part, γ_t is a complex scalar whose imaginary part ensures normalization of the wavepacket, and D is the number of coordinates. Within the thawed Gaussian approximation,⁵⁸ one replaces true potential energy $V(q)$ by its local harmonic approximation

$$V_{\text{LHA}}(q) = V(q_t) + V'(q_t)^T \cdot (q - q_t) + \frac{1}{2}(q - q_t)^T \cdot V''(q_t) \cdot (q - q_t) \quad (22)$$

about the center q_t of the wavepacket, which leads to the following equations of motion for the Gaussian’s parameters:^{58,84}

$$\dot{q}_t = m^{-1} \cdot p_t, \quad (23)$$

$$\dot{p}_t = -V'(q_t), \quad (24)$$

$$\dot{A}_t = -A_t \cdot m^{-1} \cdot A_t - V''(q_t), \quad (25)$$

$$\dot{\gamma}_t = L_t + \frac{i\hbar}{2} \text{Tr}(m^{-1} \cdot A_t), \quad (26)$$

where $L_t = p_t^T \cdot (2m)^{-1} \cdot p_t - V(q_t)$ is the Lagrangian along the trajectory (q_t, p_t) and m is the symmetric mass matrix. According to Eqs. (23)–(26), the position and momentum of the Gaussian wavepacket evolve classically, while the matrix A_t depends on the Hessians along the classical trajectory. The described evolution of the Gaussian wavepacket is exact for a harmonic potential because the local Taylor expansion of Eq. (22) becomes exact in this case. For more general, anharmonic potentials, the method is only approximate, but typically accurate for moderate anharmonicity and short times, which makes it practical in spectroscopic applications.^{58–60,85,86} Although the thawed Gaussian propagation is not suited for nonadiabatic dynamics, it can treat accurately the effects that arise due to different force constants of the ground- and excited-state potential surfaces: mode distortion, i.e., the change in the frequency of a normal mode, and intermode coupling or Duschinsky rotation. The on-the-fly ab initio thawed Gaussian approximation, which uses electronic structure calculations to compute potential energies, gradients, and Hessians only when needed, was recently validated for the simulation of finite-temperature linear⁵⁷ and zero-temperature two-dimensional spectra.⁴⁰

To construct the initial state, we approximate the ground-state potential energy surface by a harmonic potential and use the corresponding mass-scaled normal mode coordinates. Then, in the zero-temperature limit, the initial state $\psi_0(q) = \langle q|1, g \rangle$ is a Gaussian (21) and $D = F$, where F is the number of vibrational degrees of freedom. In the thermo-field dynamics formulation, $D = 2F$, the initial state $\bar{\psi}_0(\bar{q}) = \langle \bar{q}|\bar{0}(\beta) \rangle$ is also a Gaussian, and $\bar{q} = (q, \tilde{q})$ is the $2F$ -dimensional coordinate vector.⁵⁷ To solve the equations of motion in the finite-temperature picture, we need the potential energies, gradients, and Hessians in the extended coordinate space, which can be easily formulated in terms of the energies, gradients, and Hessians of the two potential energy surfaces, as shown in Ref. 57. Remarkably, the thermo-field dynamics under Hamiltonian \hat{H}_j [Eq. (14)] requires exactly the same classical trajectory, in electronic state j , as the conventional, zero-temperature thawed Gaussian propagation with Hamiltonian \hat{H}_j .⁵⁷ No further ab initio evaluations are needed for the finite-

temperature implementation, meaning that, within the thawed Gaussian approximation, the temperature effects can be included almost for free. The only difference in the computational cost is in solving the equations of motion with $2F$ rather than F coordinates, which is approximately $2^3 = 8$ times more expensive due to the roughly cubic scaling of the involved matrix operations, including matrix-matrix multiplication and matrix inverse. This cost is, however, negligible compared to the cost of electronic structure calculations.

Formally, the propagation of the wavepacket according to Eqs. (23)–(26) requires not only the potential energies and gradients but also the Hessians at each step of the dynamics. In this work, we employed the single-Hessian method,⁸⁷ which further approximates $V''(q_t) \approx V''(q_{\text{ref}})$ in Eq. (25), where q_{ref} is a reference geometry at which the Hessian of the excited-state potential surface is evaluated once and reused during the excited-state dynamics. Because the center of the wavepacket still follows the fully anharmonic classical trajectory, the single-Hessian version partially includes anharmonicity effects; in several examples studied in Ref. 87, the accuracy of this method was shown to be similar to that of the thawed Gaussian approximation. Here, we chose q_{ref} as the excited-state minimum. The ground-state potential surface was assumed to be harmonic in all simulations.

To analyze the effects of the excited-state anharmonicity, we compare the anharmonic calculations, based on the on-the-fly single-Hessian thawed Gaussian approximation for the excited-state propagation, with the harmonic model (also called the generalized Brownian oscillator model), where the excited-state potential surface is approximated by a harmonic potential fitted to the surface at its minimum (so-called adiabatic harmonic or adiabatic Hessian scheme). In the mass-scaled normal mode coordinates of the ground state, the excited-state force constant is a symmetric, non-diagonal matrix, whose off-diagonal terms reflect intermode couplings, also known as Duschinsky mixing. To study the effects of the difference between the excited- and ground-state force constants on linear and two-dimensional spectra, we construct the displaced harmonic model (also called the Brownian oscillator model), where the excited-state force constant is approximated by the force constant in the

ground electronic state. This model neglects mode distortion and Duschinsky effects. The two-dimensional spectra can be computed exactly with the thawed Gaussian propagation, as described above, for both harmonic and displaced harmonic oscillator models. Whereas the exact solution to the displaced harmonic oscillator model was known before in the form of the second-order cumulant expansion,²² to the best of our knowledge, no method has been published for computing exactly the two-dimensional spectra of the global harmonic (or generalized Brownian oscillator) model.¹⁴

Azulene is a well-known example of a Kasha-violating molecule,⁸⁸ as it emits light from the second, rather than first, excited electronic state. This is due to the interplay of two factors:⁸⁹ (i) weak nonadiabatic coupling between S_1 and S_2 states and (ii) fast (≈ 1 ps) nonradiative decay from S_1 to S_0 . These properties make azulene one of the key building blocks in the synthesis of novel optoelectronic materials.⁹⁰ Although nonadiabatic couplings between the ground and first excited states play an important role in the photoinduced dynamics of azulene,⁸⁹ they do not affect its vibrationally resolved $S_1 \leftarrow S_0$ absorption spectrum. Indeed, the linear absorption spectrum can be well reproduced using adiabatic, Born-Oppenheimer approaches that neglect nonadiabatic effects.^{89,91,92} Here, we also ignore the nonadiabatic effects on the two-dimensional spectra, which we compute only at short t_2 delay times. In the results, we focus on the ground-state bleach and stimulated emission contributions to the two-dimensional spectrum [the first two terms on the right-hand sides of Eqs. (6) and (7)]; according to the oscillator strengths of the $S_1 - S_0$ (0.009)⁹³⁻⁹⁵ and $S_2 - S_1$ ($\approx 10^{-5}$)^{94,95} transitions, the excited-state absorption is expected to be ~ 3 orders of magnitude weaker.

In Fig. 2 (top), we compare linear absorption spectra simulated at 300 and 0 K with the experimental spectrum recorded at room temperature. One of the main effects of temperature is the broadening of the spectral features, which also affects the relative intensities of vibronic peaks, namely, those at 14 300 and 15 800 cm^{-1} . These intensities are overestimated in the zero-temperature spectrum but are corrected by the finite-temperature treatment.

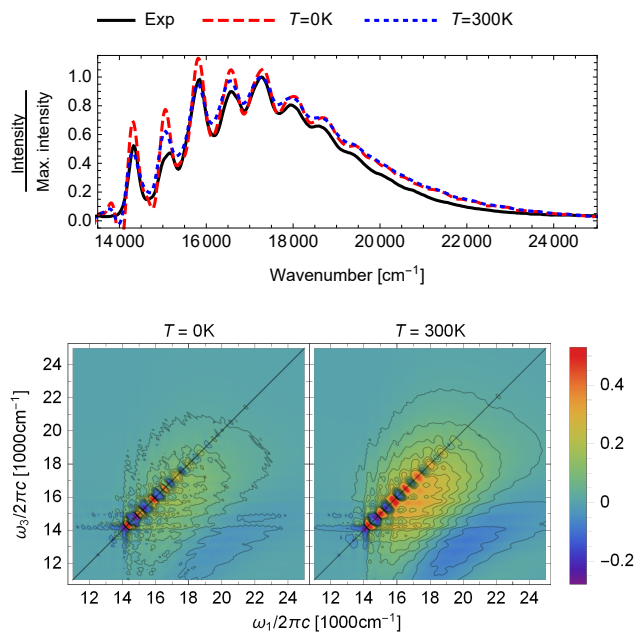


Figure 2: Top: $S_1 \leftarrow S_0$ absorption spectra of azulene computed with the on-the-fly ab initio single-Hessian thawed Gaussian approximation at zero temperature (red, dashed) and at 300 K (blue, dotted), compared with the experimental spectrum (black, solid) recorded at room temperature in cyclohexane.⁸⁹ Bottom: Absorptive two-dimensional electronic spectra [Eq. (3)] at zero delay time ($t_2 = 0$), computed at zero temperature (left) and at $T = 300$ K (right). Each spectrum shows the sum of the ground-state bleach and stimulated emission terms [first two terms on the right-hand sides of Eqs. (6) and (7)] corresponding to the S_1 - S_0 electronic transition in azulene. See Fig. S1 for the rephasing and nonrephasing contributions to these spectra and Figs. S3 and S4 of the Supporting Information for the spectra at delays $t_2 > 0$.

A non-zero temperature has an even stronger effect on the two-dimensional spectrum (Fig. 2, bottom). The zero-temperature spectrum is composed of sharp vibronic peaks, which are broadened and less resolved in the spectrum computed at 300 K. As in the linear spectrum, the temperature effects modify not only the resolution of the spectrum but also the relative intensities of the peaks. However, in contrast to the linear absorption spectrum, where these differences affect only a few peaks and could still be considered acceptable, the two-dimensional spectrum is strongly affected due to the increased complexity of spectral features.

To investigate the effects of anharmonicity, mode distortion, and mode-mode coupling, we first compare the linear absorption spectra computed using three models with different accuracies (see Fig. 3). The spectrum computed with the displaced harmonic oscillator model displays a highly regular intensity pattern, as opposed to the irregular intensities found in the experiment, and overestimates the frequency spacing between the peaks. The results are largely improved by including Duschinsky coupling and changes in the mode frequencies through the global harmonic model. However, the harmonic approximation suffers from an overly broad tail in the high-frequency region. This is further corrected by accounting for the anharmonicity effects with the on-the-fly thawed Gaussian approximation.

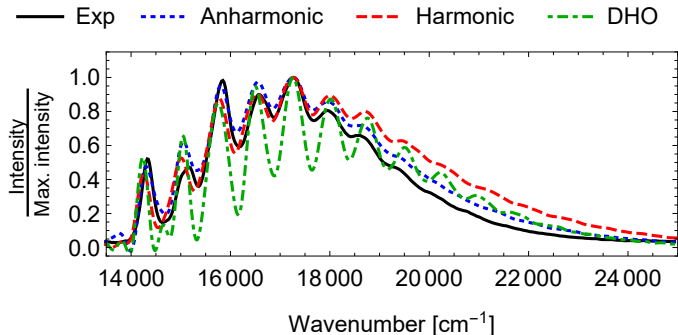


Figure 3: $S_1 \leftarrow S_0$ absorption spectra of azulene computed with the on-the-fly ab initio single-Hessian thawed Gaussian approximation (“Anharmonic”, blue, dotted), harmonic approximation (red, dashed), and the displaced harmonic oscillator (DHO) model (green, dashed-dotted) at 300 K, compared with the experimental spectrum (black, solid) recorded at room temperature in cyclohexane.⁸⁹

The corresponding two-dimensional spectra (Fig. 4, top) exhibit similar differences, which we can conveniently analyze in the time domain (see Fig. 4, bottom, for $|S_R(t_3, 0, t_1)|$ and Fig. S6 for $|S_{NR}(t_3, 0, t_1)|$). The displaced harmonic oscillator model results in stronger recurrences after 45 fs (in t_1 , t_3 , or in both t_1 and t_3) than the harmonic or anharmonic approaches. This translates into sharper peaks in the two-dimensional spectrum. The anharmonic spectrum extends less into the high frequency region, compared to the harmonic and displaced harmonic oscillator models, because the thawed Gaussian propagation gives a slower initial decay (for $t_1, t_3 < 6$ fs) in the time domain than the models that neglect anharmonicity (see Fig. S5 of the Supporting Information). Subtle differences between the harmonic and anharmonic excited-state dynamics affect the peak intensities in the region between 15 000 and 18 000 cm^{-1} .

Interestingly, for the displaced harmonic oscillator model, $|S_R(t_3, 0, t_1)|$ is symmetric with respect to the diagonal (Fig. 4, bottom right), which does not hold when mode distortion, rotation, and anharmonicity are included (Fig. 4, bottom left and middle). We prove this analytically in the Supporting Information (Secs. 7 and 8), where we also demonstrate that the asymmetry can appear only in rephasing signal $|S_R(t_3, 0, t_1)|$. Moreover, we show that the (incorrect) symmetry of $|S_R^{\text{DHO}}(t_3, 0, t_1)|$ with respect to the diagonal $t_1 = t_3$ is, more generally, imposed by the second-order cumulant approximation,²² which is exact for the displaced harmonic oscillator model and is employed regularly to model two-dimensional spectra.^{23,24,96,97} Hence, the second-order cumulant method cannot account for the asymmetry induced by the deviation from the displaced harmonic oscillator model. This erroneous qualitative behavior was difficult to study in the past, partly due to the absence of practical methods that could easily go beyond the second-order cumulants or Brownian oscillators.

To conclude, we derived a general and exact expression for computing finite-temperature vibrationally resolved two-dimensional electronic spectra with wavefunction-based methods. The inclusion of temperature is the key to simulating spectra of larger systems or solvated molecules, due to the multitude of low-frequency modes that are thermally excited at room

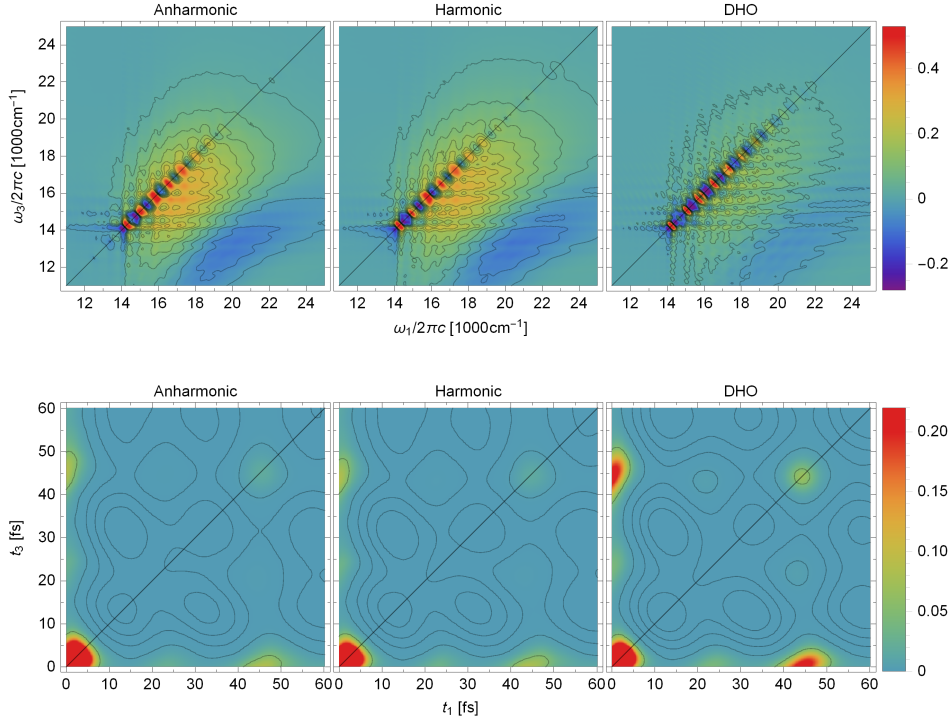


Figure 4: Top: Absorptive two-dimensional electronic spectra [Eq. (3)] at zero delay time ($t_2 = 0$), computed with the on-the-fly ab initio single-Hessian thawed Gaussian approximation (“Anharmonic”, left), harmonic approximation (middle), and the displaced harmonic oscillator (DHO) model (right) at 300 K. Each spectrum shows the sum of the ground-state bleach and stimulated emission terms [first two terms on the right-hand sides of Eqs. (6) and (7)] corresponding to the S_1 – S_0 electronic transition in azulene. See Fig. S2 for the rephasing and nonrephasing contributions to these spectra and Figs. S3 and S4 of the Supporting Information for the spectra at delays $t_2 > 0$. Bottom: First 60 fs of $|S_R(t_3, 0, t_1)|$ [Eq. (6)]. See Fig. S6 for $|S_{NR}(t_3, 0, t_1)|$.

temperature. By combining the exact expression with the thawed Gaussian approximation, we developed a practical and efficient method for computing two-dimensional spectra beyond zero temperature and beyond displaced harmonic oscillator model. With the help of the newly developed method, we identified an asymmetry in the time-domain signal that could serve as evidence for the changes in mode frequencies, mode-mode coupling, or anharmonicity. This asymmetry cannot be described with the conventional and widely used second-order cumulant approach.

Computational Methods

The ground electronic state of azulene was modeled at the second-order Møller–Plesset (MP2) perturbation theory level; the first excited state was modeled using the second-order Laplace-transformed density-fitted local algebraic diagrammatic construction [LT-DF-LADC(2)] scheme,^{98–101} as implemented in the Molpro 2015 package.¹⁰² cc-pVDZ basis set was used throughout (see Ref. 89). We first evaluated the Hessians in the ground and excited states at the respective optimized geometries. Then, starting from the minimum of the ground state, an on-the-fly ab initio classical trajectory was evolved in the excited electronic state for 1130 steps with a time step of 8 a.u. \approx 0.19 fs (total time \approx 219 fs).

Linear spectra were computed by Fourier transforming the first 500 steps of the wavepacket autocorrelation function (see Ref. 83). With regard to the simulation of two-dimensional spectra, t_1 and t_3 times were propagated up to \approx 106 fs (500 steps); t_2 delays ranged from 0 (results shown in the main text) to 25 fs (130 steps), in intervals of 5 fs or 26 steps. Condon approximation, which was justified for the $S_1 \leftarrow S_0$ absorption of azulene in Ref. 89, was employed. Gaussian broadening with a half-width at half-maximum of 90 cm^{-1} was used in both linear and two-dimensional spectra. Linear spectra were shifted in frequency and scaled in intensity to match at the maximum intensity peak of the experiment; two-dimensional spectra were shifted by the same frequency shifts as the linear absorption spectra and scaled

according to the maximum of the fully absorptive two-dimensional spectrum [Eq. (3)].

Data supporting this publication can be found at <http://doi.org/10.5281/zenodo.4552858>.

Acknowledgement

The authors acknowledge the financial support from the European Research Council (ERC) under the European Union’s Horizon 2020 research and innovation programme (grant agreement No. 683069 – MOLEQULE) and from the Swiss National Science Foundation through the NCCR MUST (Molecular Ultrafast Science and Technology) Network.

Supporting Information Available

Derivation of Eqs. (6)–(8), conjugation rules in thermo-field dynamics, thermo-field dynamics expression beyond the Born–Oppenheimer approximation, rephasing and nonrephasing contributions to the spectra of Figs. 2 (bottom) and 4 (top), two-dimensional spectra at $t_2 > 0$, $|S_R(t_3, 0, t_1)|$ at short times, (a)symmetry of the rephasing and nonrephasing spectra in the time domain, and proof of the symmetry of the two-dimensional signal within the second-order cumulant approximation.

References

- (1) Yuen-Zhou, J.; Aspuru-Guzik, A. Quantum process tomography of excitonic dimers from two-dimensional electronic spectroscopy. I. General theory and application to homodimers. *J. Chem. Phys.* **2011**, *134*, 134505.
- (2) Kreisbeck, C.; Kramer, T.; Aspuru-Guzik, A. Disentangling electronic and vibronic coherences in two-dimensional echo spectra. *J. Phys. Chem. B* **2013**, *117*, 9380–9385.

- (3) Yuen-Zhou, J.; Krich, J. J.; Kassal, I.; Johnson, A. S.; Aspuru-Guzik, A. *Ultrafast Spectroscopy*; IOP Publishing, 2014.
- (4) Zhou, N.; Chen, L.; Huang, Z.; Sun, K.; Tanimura, Y.; Zhao, Y. Fast, Accurate Simulation of Polaron Dynamics and Multidimensional Spectroscopy by Multiple Davydov Trial States. *J. Phys. Chem. A* **2016**, *120*, 1562–1576.
- (5) Ikeda, T.; Tanimura, Y. Probing photoisomerization processes by means of multi-dimensional electronic spectroscopy: The multi-state quantum hierarchical Fokker-Planck equation approach. *J. Chem. Phys.* **2017**, *147*, 014102.
- (6) Xiang, B.; Ribeiro, R. F.; Dunkelberger, A. D.; Wang, J.; Li, Y.; Simpkins, B. S.; Owrutsky, J. C.; Yuen-Zhou, J.; Xiong, W. Two-dimensional infrared spectroscopy of vibrational polaritons. *Proc. Nat. Acad. Sci. USA* **2018**, *115*, 4845–4850.
- (7) Conti, I.; Cerullo, G.; Nenov, A.; Garavelli, M. Ultrafast Spectroscopy of Photoactive Molecular Systems from First Principles : Where We Stand Today and Where We Are Going. *J. Am. Chem. Soc.* **2020**, *142*, 16117.
- (8) Kano, H.; Saito, T.; Kobayashi, T. Observation of Herzberg-Teller-type wave packet motion in porphyrin J-aggregates studied by sub-5-fs spectroscopy. *J. Phys. Chem. A* **2002**, *106*, 3445–3453.
- (9) Kobayashi, T.; Wang, Z.; Otsubo, T. Classification of dynamic vibronic couplings in vibrational real-time spectra of a thiophene derivative by few-cycle pulses. *J. Phys. Chem. A* **2007**, *111*, 12985–12994.
- (10) Fidler, A. F.; Engel, G. S. Nonlinear spectroscopic theory of displaced harmonic oscillators with differing curvatures: A correlation function approach. *J. Phys. Chem. A* **2013**, *117*, 9444–9453.

- (11) Bizimana, L. A.; Carbery, W. P.; Gellen, T. A.; Turner, D. B. Signatures of Herzberg-Teller coupling in three-dimensional electronic spectroscopy. *J. Chem. Phys.* **2017**, *146*, 084311.
- (12) Anda, A.; Abramavičius, D.; Hansen, T. Two-dimensional electronic spectroscopy of anharmonic molecular potentials. *Phys. Chem. Chem. Phys.* **2018**, *20*, 1642–1652.
- (13) Zuehlsdorff, T. J.; Montoya-Castillo, A.; Napoli, J. A.; Markland, T. E.; Isborn, C. M. Optical spectra in the condensed phase: Capturing anharmonic and vibronic features using dynamic and static approaches. *J. Chem. Phys.* **2019**, *151*, 074111.
- (14) Zuehlsdorff, T. J.; Hong, H.; Shi, L.; Isborn, C. M. Nonlinear spectroscopy in the condensed phase: The role of Duschinsky rotations and third order cumulant contributions. *J. Chem. Phys.* **2020**, *153*, 044127.
- (15) Shedge, S. V.; Zuehlsdorff, T. J.; Khanna, A.; Conley, S.; Isborn, C. M. Explicit environmental and vibronic effects in simulations of linear and nonlinear optical spectroscopy Explicit environmental and vibronic effects in simulations of linear and nonlinear optical spectroscopy. *J. Chem. Phys.* **2021**, *084116*, 084116.
- (16) Fuji, T.; Saito, T.; Kobayashi, T. Dynamical observation of Duschinsky rotation by sub-5-fs real-time spectroscopy. *Chem. Phys. Lett.* **2000**, *332*, 324–330.
- (17) Bizimana, L. A.; Brazard, J.; Carbery, W. P.; Gellen, T.; Turner, D. B. Resolving molecular vibronic structure using high-sensitivity two-dimensional electronic spectroscopy. *J. Chem. Phys.* **2015**, *143*, 164203.
- (18) Galestian Pour, A.; Lincoln, C. N.; Perlík, V.; Šanda, F.; Hauer, J. Anharmonic vibrational effects in linear and two-dimensional electronic spectra. *Phys. Chem. Chem. Phys.* **2017**, *19*, 24752–24760.

- (19) Zhu, R.; Zou, J.; Wang, Z.; Chen, H.; Weng, Y. Electronic state-resolved multimode-coupled vibrational wavepackets in oxazine 720 by two-dimensional electronic spectroscopy. *J. Phys. Chem. A* **2020**, *124*, 9333–9342.
- (20) Fumero, G.; Schnedermann, C.; Batignani, G.; Wende, T.; Liebel, M.; Bassolino, G.; Ferrante, C.; Mukamel, S.; Kukura, P.; Scopigno, T. Two-dimensional impulsively stimulated resonant Raman spectroscopy of molecular excited states. *Phys. Rev. X* **2020**, *10*, 11051.
- (21) Mukamel, S. Dressed-cluster and hydrodynamic expansions for line broadening in simple fluids. *Phys. Rev. A* **1982**, *26*, 617.
- (22) Mukamel, S. *Principles of nonlinear optical spectroscopy*, 1st ed.; Oxford University Press: New York, 1999.
- (23) Segarra-Martí, J.; Mukamel, S.; Garavelli, M.; Nenov, A.; Rivalta, I. Towards Accurate Simulation of Two-Dimensional Electronic Spectroscopy. *Top. Curr. Chem.* **2018**, *376*, 24.
- (24) Picchiotti, A.; Nenov, A.; Giussani, A.; Prokhorenko, V. I.; Miller, R. J. D.; Mukamel, S.; Garavelli, M. Pyrene, a Test Case for Deep-Ultraviolet Molecular Photophysics. *J. Phys. Chem. Lett.* **2019**, *10*, 3481–3487.
- (25) Mukamel, S. On the semiclassical calculation of molecular absorption and fluorescence spectra. *J. Chem. Phys.* **1982**, *77*, 173–181.
- (26) Egorov, S. A.; Rabani, E.; Berne, B. J. Vibronic spectra in condensed matter: A comparison of exact quantum mechanical and various semiclassical treatments for harmonic baths. *J. Chem. Phys.* **1998**, *108*, 1407–1422.
- (27) Egorov, S. A.; Rabani, E.; Berne, B. J. Nonradiative relaxation processes in condensed phases: Quantum versus classical baths. *J. Chem. Phys.* **1999**, *110*, 5238–5248.

- (28) Shi, Q.; Geva, E. A derivation of the mixed quantum-classical Liouville equation from the influence functional formalism. *J. Chem. Phys.* **2004**, *121*, 3393–3404.
- (29) McRobbie, P. L.; Hanna, G.; Shi, Q.; Geva, E. Signatures of nonequilibrium solvation dynamics on multidimensional spectra. *Acc. Chem. Res.* **2009**, *42*, 1299–1309.
- (30) McRobbie, P. L.; Geva, E. A benchmark study of different methods for calculating one- and two-dimensional optical spectra. *J. Phys. Chem. A* **2009**, *113*, 10425–10434.
- (31) Mollica, C.; Vaníček, J. Beating the Efficiency of Both Quantum and Classical Simulations with a Semiclassical Method. *Phys. Rev. Lett.* **2011**, *107*, 214101.
- (32) Wehrle, M.; Šulc, M.; Vaníček, J. Time-Resolved Electronic Spectra with Efficient Quantum Dynamics Methods. *Chimia* **2011**, *65*, 334–338.
- (33) Šulc, M.; Vaníček, J. Accelerating the calculation of time-resolved electronic spectra with the cellular dephasing representation. *Mol. Phys.* **2012**, *110*, 945–955.
- (34) Zambrano, E.; Šulc, M.; Vaníček, J. Improving the accuracy and efficiency of time-resolved electronic spectra calculations: Cellular dephasing representation with a prefactor. *J. Chem. Phys.* **2013**, *139*, 054109.
- (35) Schubert, A.; Engel, V. Two-dimensional vibronic spectroscopy of coherent wavepacket motion. *J. Chem. Phys.* **2011**, *134*, 104304.
- (36) Krčmář, J.; Gelin, M. F.; Domcke, W. Calculation of third-order signals via driven Schrödinger equations: General results and application to electronic 2D photon echo spectroscopy. *Chem. Phys.* **2013**, *422*, 53–62.
- (37) Krčmář, J.; Gelin, M. F.; Domcke, W. Simulation of femtosecond two-dimensional electronic spectra of conical intersections. *J. Chem. Phys.* **2015**, *143*, 074308.

- (38) Picconi, D.; Cina, J. A.; Burghardt, I. Quantum dynamics and spectroscopy of dihalogens in solid matrices. I. Efficient simulation of the photodynamics of the embedded I_2Kr_{18} cluster using the G-MCTDH method. *J. Chem. Phys.* **2019**, *150*, 064111.
- (39) Picconi, D.; Cina, J. A.; Burghardt, I. Quantum dynamics and spectroscopy of dihalogens in solid matrices. II. Theoretical aspects and G-MCTDH simulations of time-resolved coherent Raman spectra of Schrödinger cat states of the embedded I_2Kr_{18} cluster. *J. Chem. Phys.* **2019**, *150*, 064112.
- (40) Begušić, T.; Vaníček, J. On-the-fly ab initio semiclassical evaluation of third-order response functions for two-dimensional electronic spectroscopy. *J. Chem. Phys.* **2020**, *153*, 184110.
- (41) Matzkies, F.; Manthe, U. Accurate reaction rate calculations including internal and rotational motion: A statistical multi-configurational time-dependent Hartree approach. *J. Chem. Phys.* **1999**, *110*, 88–96.
- (42) Manthe, U.; Huarte-Larrañaga, F. Partition functions for reaction rate calculations: Statistical sampling and MCTDH propagation. *Chem. Phys. Lett.* **2001**, *349*, 321–328.
- (43) Gelman, D.; Kosloff, R. Simulating dissipative phenomena with a random phase thermal wavefunctions, high temperature application of the Surrogate Hamiltonian approach. *Chem. Phys. Lett.* **2003**, *381*, 129–138.
- (44) Nest, M.; Kosloff, R. Quantum dynamical treatment of inelastic scattering of atoms at a surface at finite temperature: The random phase thermal wave function approach. *J. Chem. Phys.* **2007**, *127*, 134711.
- (45) Lorenz, U.; Saalfrank, P. Comparing thermal wave function methods for multi-configuration time-dependent Hartree simulations. *J. Chem. Phys.* **2014**, *140*, 044106.

- (46) Wang, L.; Fujihashi, Y.; Chen, L.; Zhao, Y. Finite-temperature time-dependent variation with multiple Davydov states. *J. Chem. Phys.* **2017**, *146*, 124127.
- (47) Werther, M.; Grossmann, F. Including temperature in a wavefunction description of the dynamics of the quantum Rabi model. *J. Phys. A: Math. Theor.* **2018**, 014001.
- (48) Suzuki, M. Thermo Field Dynamics in Equilibrium and Non-Equilibrium Interacting Quantum Systems. *J. Phys. Soc. Jap.* **1985**, *54*, 4483–4485.
- (49) Takahashi, Y.; Umezawa, H. Thermo Field Dynamics. *Int. J. Mod. Phys. B* **1996**, *10*, 1755–1805.
- (50) Harsha, G.; Henderson, T. M.; Scuseria, G. E. Thermofield Theory for Finite-Temperature Coupled Cluster. *J. Chem. Theory Comput.* **2019**, *15*, 6127–6136.
- (51) Harsha, G.; Henderson, T. M.; Scuseria, G. E. Thermofield theory for finite-temperature quantum chemistry. *J. Chem. Phys.* **2019**, *150*, 154109.
- (52) Shushkov, P.; Miller, T. F. Real-time density-matrix coupled-cluster approach for closed and open systems at finite temperature. *J. Chem. Phys.* **2019**, *151*, 134107.
- (53) Borrelli, R.; Gelin, M. F. Quantum electron-vibrational dynamics at finite temperature: Thermo field dynamics approach. *J. Chem. Phys.* **2016**, *145*, 224101.
- (54) Borrelli, R.; Gelin, M. F. Simulation of Quantum Dynamics of Excitonic Systems at Finite Temperature: An efficient method based on Thermo Field Dynamics. *Sci. Rep.* **2017**, *7*, 9127.
- (55) Gelin, M. F.; Borrelli, R. Thermal Schrödinger Equation: Efficient Tool for Simulation of Many-Body Quantum Dynamics at Finite Temperature. *Annalen der Physik* **2017**, *529*, 1700200.
- (56) Chen, L.; Zhao, Y. Finite temperature dynamics of a Holstein polaron: The thermo-field dynamics approach. *J. Chem. Phys.* **2017**, *147*, 214102.

- (57) Begušić, T.; Vaníček, J. On-the-fly ab initio semiclassical evaluation of vibronic spectra at finite temperature. *J. Chem. Phys.* **2020**, *153*, 024105.
- (58) Heller, E. J. Time-dependent approach to semiclassical dynamics. *J. Chem. Phys.* **1975**, *62*, 1544–1555.
- (59) Wehrle, M.; Šulc, M.; Vaníček, J. On-the-fly Ab Initio Semiclassical Dynamics: Identifying Degrees of Freedom Essential for Emission Spectra of Oligothiophenes. *J. Chem. Phys.* **2014**, *140*, 244114.
- (60) Wehrle, M.; Oberli, S.; Vaníček, J. On-the-fly ab initio semiclassical dynamics of floppy molecules: Absorption and photoelectron spectra of ammonia. *J. Phys. Chem. A* **2015**, *119*, 5685.
- (61) Schlau-Cohen, G. S.; Ishizaki, A.; Fleming, G. R. Two-dimensional electronic spectroscopy and photosynthesis: Fundamentals and applications to photosynthetic light-harvesting. *Chem. Phys.* **2011**, *386*, 1–22.
- (62) Khalil, M.; Demirdöven, N.; Tokmakoff, A. Obtaining absorptive line shapes in two-dimensional infrared vibrational correlation spectra. *Phys. Rev. Lett.* **2003**, *90*, 4.
- (63) Johnson, P. J. M.; Koziol, K. L.; Hamm, P. Intrinsic phasing of heterodyne-detected multidimensional infrared spectra. *Opt. Express* **2017**, *25*, 2928.
- (64) Meyer, H.-D., Gatti, F., Worth, G. A., Eds. *Multidimensional Quantum Dynamics: MCTDH Theory and Applications*, 1st ed.; Wiley-VCH: Weinheim, 2009.
- (65) Roulet, J.; Choi, S.; Vaníček, J. Efficient geometric integrators for nonadiabatic quantum dynamics. II. The diabatic representation. *J. Chem. Phys.* **2019**, *150*, 204113.
- (66) Choi, S.; Vaníček, J. Efficient geometric integrators for nonadiabatic quantum dynamics. I. The adiabatic representation. *J. Chem. Phys.* **2019**, *150*, 204112.

- (67) Choi, S.; Vaníček, J. A time-reversible integrator for the time-dependent Schrödinger equation on an adaptive grid. *J. Chem. Phys.* **2019**, *151*, 234102.
- (68) Tatchen, J.; Pollak, E. Semiclassical on-the-fly computation of the $S_0 \rightarrow S_1$ absorption spectrum of formaldehyde. *J. Chem. Phys.* **2009**, *130*, 041103.
- (69) Conte, R.; Ceotto, M. In *Quantum chemistry and dynamics of excited states*; González, L., Lindh, R., Eds.; John Wiley & Sons, Ltd, 2020; Chapter 19, pp 595–628.
- (70) Buchholz, M.; Grossmann, F.; Ceotto, M. Mixed semiclassical initial value representation time-averaging propagator for spectroscopic calculations. *J. Chem. Phys.* **2016**, *144*, 094102.
- (71) Buchholz, M.; Grossmann, F.; Ceotto, M. Application of the mixed time-averaging semiclassical initial value representation method to complex molecular spectra. *J. Chem. Phys.* **2017**, *147*, 164110.
- (72) Curchod, B. F. E.; Martínez, T. J. Ab Initio Nonadiabatic Quantum Molecular Dynamics. *Chem. Rev.* **2018**, *118*, 3305–3336.
- (73) Makhov, D. V.; Glover, W. J.; Martinez, T. J.; Shalashilin, D. V. Ab initio multiple cloning algorithm for quantum nonadiabatic molecular dynamics. *J. Chem. Phys.* **2014**, *141*, 054110.
- (74) Makhov, D. V.; Symonds, C.; Fernandez-Alberti, S.; Shalashilin, D. V. Ab initio quantum direct dynamics simulations of ultrafast photochemistry with Multiconfigurational Ehrenfest approach. *Chem. Phys.* **2017**, *493*, 200–218.
- (75) Thompson, A. L.; Martínez, T. J. Time-resolved photoelectron spectroscopy from first principles: Excited state dynamics of benzene. *Faraday Discuss.* **2011**, *150*, 293–311.
- (76) Šulc, M.; Hernández, H.; Martínez, T. J.; Vaníček, J. Relation of exact Gaussian basis

- methods to the dephasing representation: Theory and application to time-resolved electronic spectra. *J. Chem. Phys.* **2013**, *139*, 034112.
- (77) Zimmermann, T.; Vaníček, J. Efficient on-the-fly ab initio semiclassical method for computing time-resolved nonadiabatic electronic spectra with surface hopping or Ehrenfest dynamics. *J. Chem. Phys.* **2014**, *141*, 134102.
- (78) Worth, G. A.; Robb, M. A.; Burghardt, I. A novel algorithm for non-adiabatic direct dynamics using variational Gaussian wavepackets. *Faraday Discuss.* **2004**, *127*, 307–323.
- (79) Richings, G. W.; Polyak, I.; Spinlove, K. E.; Worth, G. A.; Burghardt, I.; Lasorne, B. Quantum Dynamics Simulations Using Gaussian Wavepackets: the vMCG Method. *Int. Rev. Phys. Chem.* **2015**, *34*, 269–308.
- (80) Bonfanti, M.; Petersen, J.; Eisenbrandt, P.; Burghardt, I.; Pollak, E. Computation of the S1 S0 vibronic absorption spectrum of formaldehyde by variational Gaussian wavepacket and semiclassical IVR methods. *J. Chem. Theory Comput.* **2018**, *14*, 5310–4323.
- (81) Polyak, I.; Richings, G. W.; Habershon, S.; Knowles, P. J. Direct quantum dynamics using variational Gaussian wavepackets and Gaussian process regression. *J. Chem. Phys.* **2019**, *150*, 041101.
- (82) Chen, L.; Sun, K.; Shalashilin, D. V.; Gelin, M. F.; Zhao, Y. Efficient simulation of time- and frequency-resolved four-wave-mixing signals with a multiconfigurational Ehrenfest approach. *J. Chem. Phys.* **2021**, *154*, 054105.
- (83) Vaníček, J.; Begušić, T. In *Molecular Spectroscopy and Quantum Dynamics*; Marquardt, R., Quack, M., Eds.; Elsevier, 2021; pp 199–229.

- (84) Lasser, C.; Lubich, C. Computing quantum dynamics in the semiclassical regime. *Acta Numerica* **2020**, *29*, 229–401.
- (85) Rohrdanz, M. A.; Cina, J. A. Probing intermolecular communication via lattice phonons with time-resolved coherent anti-Stokes Raman scattering. *Mol. Phys.* **2006**, *104*, 1161–1178.
- (86) Begušić, T.; Roulet, J.; Vaníček, J. On-the-fly ab initio semiclassical evaluation of time-resolved electronic spectra. *J. Chem. Phys.* **2018**, *149*, 244115.
- (87) Begušić, T.; Cordova, M.; Vaníček, J. Single-Hessian thawed Gaussian approximation. *J. Chem. Phys.* **2019**, *150*, 154117.
- (88) Beer, M.; Longuet-Higgins, H. C. Anomalous light emission of azulene. *J. Chem. Phys.* **1955**, *23*, 1390–1391.
- (89) Prlj, A.; Begušić, T.; Zhang, Z. T.; Fish, G. C.; Wehrle, M.; Zimmermann, T.; Choi, S.; Roulet, J.; Moser, J.-E.; Vaníček, J. Semiclassical Approach to Photophysics Beyond Kasha’s Rule and Vibronic Spectroscopy Beyond the Condon Approximation. The Case of Azulene. *J. Chem. Theory Comput.* **2020**, *16*, 2617–2626.
- (90) Xin, H.; Gao, X. Application of azulene in constructing organic optoelectronic materials: New tricks for an old dog. *Chempluschem* **2017**, *82*, 945–956.
- (91) Dierksen, M.; Grimme, S. Density functional calculations of the vibronic structure of electronic absorption spectra. *J. Chem. Phys.* **2004**, *120*, 3544–3554.
- (92) Niu, Y.; Peng, Q.; Deng, C.; Gao, X.; Shuai, Z. Theory of excited state decays and optical spectra: Application to polyatomic molecules. *J. Phys. Chem. A* **2010**, *114*, 7817–7831.
- (93) Thulstrup, E. W.; Case, P. L.; Michl, J. Azulene: polarized absorption in stretched polymers and magnetic circular dichroism. *Chem. Phys.* **1974**, *6*, 410–418.

- (94) Gillispie, G. D.; Lim, E. C. Vibrational analysis of the S2-S1 fluorescence of azulene in a naphthalene mixed crystal at 4.2 K. *J. Chem. Phys.* **1978**, *68*, 4578–4586.
- (95) Foggi, P.; Neuwahl, F. V. R.; Moroni, L.; Salvi, P. R. S1-Sn and S2-Sn Absorption of Azulene: Femtosecond Transient Spectra and Excited State Calculations. *J. Phys. Chem. A* **2003**, *107*, 1689–1696.
- (96) Nenov, A.; Giussani, A.; Fingerhut, B. P.; Rivalta, I.; Dumont, E.; Mukamel, S.; Garavelli, M. Spectral lineshapes in nonlinear electronic spectroscopy. *Phys. Chem. Chem. Phys.* **2015**, *17*, 30925–30936.
- (97) Farfan, C. A.; Turner, D. B. Interference among multiple vibronic modes in two-dimensional electronic spectroscopy. *Mathematics* **2020**, *8*, 157.
- (98) Kats, D.; Schütz, M. A multistate local coupled cluster CC2 response method based on the Laplace transform. *J. Chem. Phys.* **2009**, *131*, 124117.
- (99) Ledermüller, K.; Kats, D.; Schütz, M. Local CC2 response method based on the Laplace transform: Orbital-relaxed first-order properties for excited states. *J. Chem. Phys.* **2013**, *139*, 084111.
- (100) Ledermüller, K.; Schütz, M. Local CC2 response method based on the Laplace transform: Analytic energy gradients for ground and excited states. *J. Chem. Phys.* **2014**, *140*, 164113.
- (101) Schütz, M. Oscillator strengths, first-order properties, and nuclear gradients for local ADC(2). *J. Chem. Phys.* **2015**, *142*, 214103.
- (102) Werner, H.-J.; Knowles, P. J.; Knizia, G.; Manby, F. R.; Schütz, M.; Celani, P.; Györffy, W.; Kats, D.; Korona, T.; Lindh, R. et al. MOLPRO, version 2015.1, a package of ab initio programs. 2015; see "<http://www.molpro.net>".

Supporting Information:

**Finite-temperature, Anharmonicity, and
Duschinsky Effects on the Two-dimensional
Electronic Spectra from Ab Initio Thermo-field
Gaussian Wavepacket Dynamics**

Tomislav Begušić* and Jiří Vaníček*

*Laboratory of Theoretical Physical Chemistry, Institut des Sciences et Ingénierie Chimiques,
Ecole Polytechnique Fédérale de Lausanne (EPFL), CH-1015, Lausanne, Switzerland*

E-mail: tomislav.begusic@epfl.ch; jiri.vanicek@epfl.ch

1 Rephasing and nonrephasing signals for a three-level system within the Born-Oppenheimer approximation

Since the Eqs. (6)–(8) of the main text are rarely found in that form, let us summarize how they can be obtained from the expressions that are easily found in the literature. The third-order response function^{S1,S2}

$$R^{(3)}(t_3, t_2, t_1) = \sum_{\alpha=1}^4 [R_{\alpha}(t_3, t_2, t_1) - R_{\alpha}(t_3, t_2, t_1)^*] \quad (1)$$

can be expressed in terms of correlation functions

$$R_1(t_3, t_2, t_1) = C(t_2, t_3, t_1 + t_2 + t_3), \quad (2)$$

$$R_2(t_3, t_2, t_1) = C(t_1 + t_2, t_3, t_2 + t_3), \quad (3)$$

$$R_3(t_3, t_2, t_1) = C(t_1, t_2 + t_3, t_3), \quad (4)$$

$$R_4(t_3, t_2, t_1) = C(-t_3, -t_2, t_1), \quad (5)$$

where

$$C(\tau_a, \tau_b, \tau_c) = \text{Tr}[\hat{\boldsymbol{\rho}}\hat{\boldsymbol{\mu}}e^{i\hat{\mathbf{H}}\tau_a/\hbar}\hat{\boldsymbol{\mu}}e^{i\hat{\mathbf{H}}\tau_b/\hbar}\hat{\boldsymbol{\mu}}e^{-i\hat{\mathbf{H}}\tau_c/\hbar}\hat{\boldsymbol{\mu}}e^{-i\hat{\mathbf{H}}(\tau_a+\tau_b-\tau_c)/\hbar}]. \quad (6)$$

In Eq. (6), we use the bold font to denote $S \times S$ matrices representing operators acting on the electronic subspace and hat $\hat{}$ to denote operators acting on the nuclear subspace; the trace is taken over both nuclear and electronic degrees of freedom. Hence, $\hat{\boldsymbol{\rho}} = \exp(-\beta\hat{\mathbf{H}})/\text{Tr}[\exp(-\beta\hat{\mathbf{H}})]$ is the full molecular density matrix, $\hat{\mathbf{H}}$ is the molecular Hamiltonian, and $\hat{\boldsymbol{\mu}}$ is the dipole moment matrix. Equations (2)–(6) can be easily compared to those found in the literature, for example, with Eqs. (3.5a)–(3.6) of Ref. S2.

We now consider only three electronic states and invoke the following approximations:

1. Born-Oppenheimer approximation: $\hat{\mathbf{H}} = \text{diag}(\hat{H}_1, \hat{H}_2, \hat{H}_3)$.
2. Resonance condition: Only transitions between states 1 and 2 or 2 and 3 are allowed:

$$\hat{\boldsymbol{\mu}} = \begin{pmatrix} 0 & \hat{\mu}_{21} & 0 \\ \hat{\mu}_{12} & 0 & \hat{\mu}_{23} \\ 0 & \hat{\mu}_{32} & 0 \end{pmatrix}. \quad (7)$$

3. The system is initially in the ground electronic state, i.e., the temperature effects on the electronic subspace are neglected: $\hat{\boldsymbol{\rho}} = \text{diag}(\hat{\rho}, 0, 0)$, where $\hat{\rho} = \exp(-\beta\hat{H}_1)/\text{Tr}[\exp(-\beta\hat{H}_1)]$.

Then, we take the trace over the electronic subspace in Eq. (6) to arrive at

$$C(\tau_a, \tau_b, \tau_c) \approx C_1(\tau_a, \tau_b, \tau_c) + C_3(\tau_a, \tau_b, \tau_c), \quad (8)$$

where C_1 and C_3 are defined according to Eq. (8) of the main text.

Finally, as discussed in Ref. S2, under the rotating-wave approximation, the rephasing and nonrephasing signals are given by

$$S_{\text{R}}(t_3, t_2, t_1) = R_2(t_3, t_2, t_1) + R_3(t_3, t_2, t_1) - R_1(t_3, t_2, t_1)^*, \quad (9)$$

$$S_{\text{NR}}(t_3, t_2, t_1) = R_1(t_3, t_2, t_1) + R_4(t_3, t_2, t_1) - R_2(t_3, t_2, t_1)^*. \quad (10)$$

Although each R_α splits into two terms of the right-hand side of Eq. (8), only one of those terms remains under the rotating-wave approximation. Therefore, Eqs. (9) and (10) lead to Eqs. (6) and (7) of the main text.

2 Conjugation rules in thermo-field dynamics

In the main text, we have introduced the fictitious Hilbert space with an orthonormal basis $\{|\tilde{k}\rangle\}$, which is related to the physical system (with the orthonormal basis $\{|k\rangle\}$) through

the conjugation rules^{S3}

$$(\hat{A}\hat{B})^\sim = \hat{\tilde{A}}\hat{\tilde{B}}, \quad (11)$$

$$(\hat{A}|\alpha\rangle)^\sim = \hat{\tilde{A}}|\tilde{\alpha}\rangle, \quad (12)$$

$$(a\hat{A} + b\hat{B})^\sim = a^*\hat{\tilde{A}} + b^*\hat{\tilde{B}}, \quad (13)$$

$$(a|\alpha\rangle + b|\beta\rangle)^\sim = a^*|\tilde{\alpha}\rangle + b^*|\tilde{\beta}\rangle, \quad (14)$$

where the operators (\hat{A} , \hat{B}) act on and states ($|\alpha\rangle$, $|\beta\rangle$) belong to the original (without tilde) or fictitious (with tilde) Hilbert spaces; a and b are complex numbers.

Let $|\alpha\rangle = \sum_k a_k |k\rangle$. Then, $|\tilde{\alpha}\rangle = \sum_k a_k^* |\tilde{k}\rangle$,

$$\langle \tilde{\alpha} | \tilde{\beta} \rangle = \sum_k a_k b_k^* = \langle \beta | \alpha \rangle, \quad (15)$$

and

$$\langle \tilde{\alpha}' | \hat{\tilde{A}} | \tilde{\alpha} \rangle = \langle \tilde{\alpha}' | \hat{\tilde{A}} \tilde{\alpha} \rangle = \langle \hat{A} \alpha | \alpha' \rangle = \langle \alpha | \hat{A}^\dagger | \alpha' \rangle, \quad (16)$$

where in the second step of Eq. (16) we used Eqs. (12) and (15).

We now complete the proof of the main text, namely the step connecting Eqs. (17) and (18) of the main text, as follows:

$$\langle \tilde{k}_1 | e^{-i\hat{H}_1(\tau_a + \tau_b - \tau_c)/\hbar} | \tilde{k}_2 \rangle = \langle \tilde{k}_1 | \left[e^{i\hat{H}_1(\tau_a + \tau_b - \tau_c)/\hbar} \right]^\sim | \tilde{k}_2 \rangle \quad (17)$$

$$= \langle k_2 | \left[e^{i\hat{H}_1(\tau_a + \tau_b - \tau_c)/\hbar} \right]^\dagger | k_1 \rangle \quad (18)$$

$$= \langle k_2 | e^{-i\hat{H}_1(\tau_a + \tau_b - \tau_c)/\hbar} | k_1 \rangle, \quad (19)$$

where in (17) we used the conjugation rules (11) and (13), in going from (17) to (18) we used Eq. (16), and in the last step we used the fact that the Hamiltonian is Hermitian.

3 Thermo-field dynamics expression for $C(\tau_a, \tau_b, \tau_c)$ beyond the Born-Oppenheimer approximation

In the main text, we invoked the Born–Oppenheimer approximation so that the thermo-field dynamics expression could be easily combined with the thawed Gaussian wavepacket dynamics. Of course, in many systems of interest, such as excitonic or multichromophoric systems, or photochemically active molecules, the coupling between electronic states must be included in the calculations. Here, we present the result beyond the Born-Oppenheimer approximation.

As in Eq. (11) of the main text, we define the thermal vacuum, now in the extended molecular (electronic and vibrational) Hilbert space:

$$|\bar{\mathbf{0}}(\beta)\rangle = \hat{\rho}^{1/2} \sum_k |\mathbf{k}\tilde{\mathbf{k}}\rangle. \quad (20)$$

In other words, the state $|\bar{\mathbf{0}}(\beta)\rangle$ is described not only by a doubled number of vibrational coordinates, but also a doubled number of electronic degrees of freedom. Following similar steps as in the derivation of the main text, we can rewrite Eq. (6) (see Sec. 1 of the Supporting Information) as

$$C(\tau_a, \tau_b, \tau_c) = \langle \bar{\phi}_{\tau_b, \tau_a} | \bar{\phi}_{0, \tau_c} \rangle, \quad (21)$$

where

$$|\bar{\phi}_{\tau, t}\rangle = e^{-i\hat{\mathbf{H}}\tau/\hbar} \hat{\mu} e^{-i\hat{\mathbf{H}}t/\hbar} \hat{\mu} |\bar{\mathbf{0}}(\beta)\rangle \quad (22)$$

and $\hat{\mathbf{H}} = \hat{\mathbf{H}} - \hat{\mathbf{H}}$. The result (21) accounts for coupled electronic states and thermal population of excited electronic states. Importantly, Eq. (21) justifies the thermo-field wavepacket picture even beyond the Born–Oppenheimer approximation.

4 Rephasing and nonrephasing two-dimensional spectra

In Figs. S1 and S2, we show separately the rephasing and nonrephasing contributions to the total absorptive spectra of the main text. The rephasing spectrum exhibits a “checkerboard” pattern,^{S4,S5} whereas the nonrephasing peaks appear only along the diagonal.^{S6} The interesting nodal structure of the nonrephasing spectrum at $t_2 = 0$ is a consequence of the broadening. As discussed in Refs. S7 and S2, the peak lineshape exhibits a “phase twist” due to the so-called dispersive component of the broadening function. In the nonrephasing spectrum, the negative intensities about a peak centered at (Ω_1, Ω_3) appear at $(\omega_1 > \Omega_1, \omega_3 > \Omega_3)$ and $(\omega_1 < \Omega_1, \omega_3 < \Omega_3)$ [see, e.g., Fig. 3(b) of Ref. S2]. By simple addition, these negative features become enhanced in between the diagonal peaks (see Fig. S2, bottom). Contrary to general knowledge, this nodal structure does not disappear when we sum the rephasing and nonrephasing spectra (see, e.g., Fig. S3, top). Due to coherent vibrational dynamics, the nonrephasing and rephasing spectra are different. More precisely, the diagonal peaks of the nonrephasing spectrum are much stronger than the same peaks in the rephasing spectrum and, therefore, their dispersive contributions do not cancel out completely in the total spectrum.^{S2,S7} Consequently, the total spectrum, given by the sum of the rephasing and nonrephasing spectra, is not necessarily composed of purely absorptive peaks. Similar pattern can be seen, for example, in Fig. 4 (leftmost panels showing spectra at $t_2 = 0$) of Ref. S8.

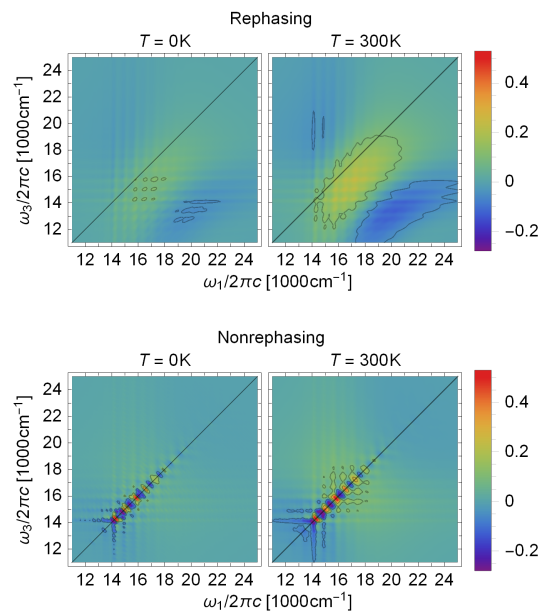


Figure S1: Rephasing (top) and nonrephasing (bottom) contributions to the two-dimensional spectra from Fig. 2 of the main text at zero temperature (left) and at $T = 300\text{K}$ (right).

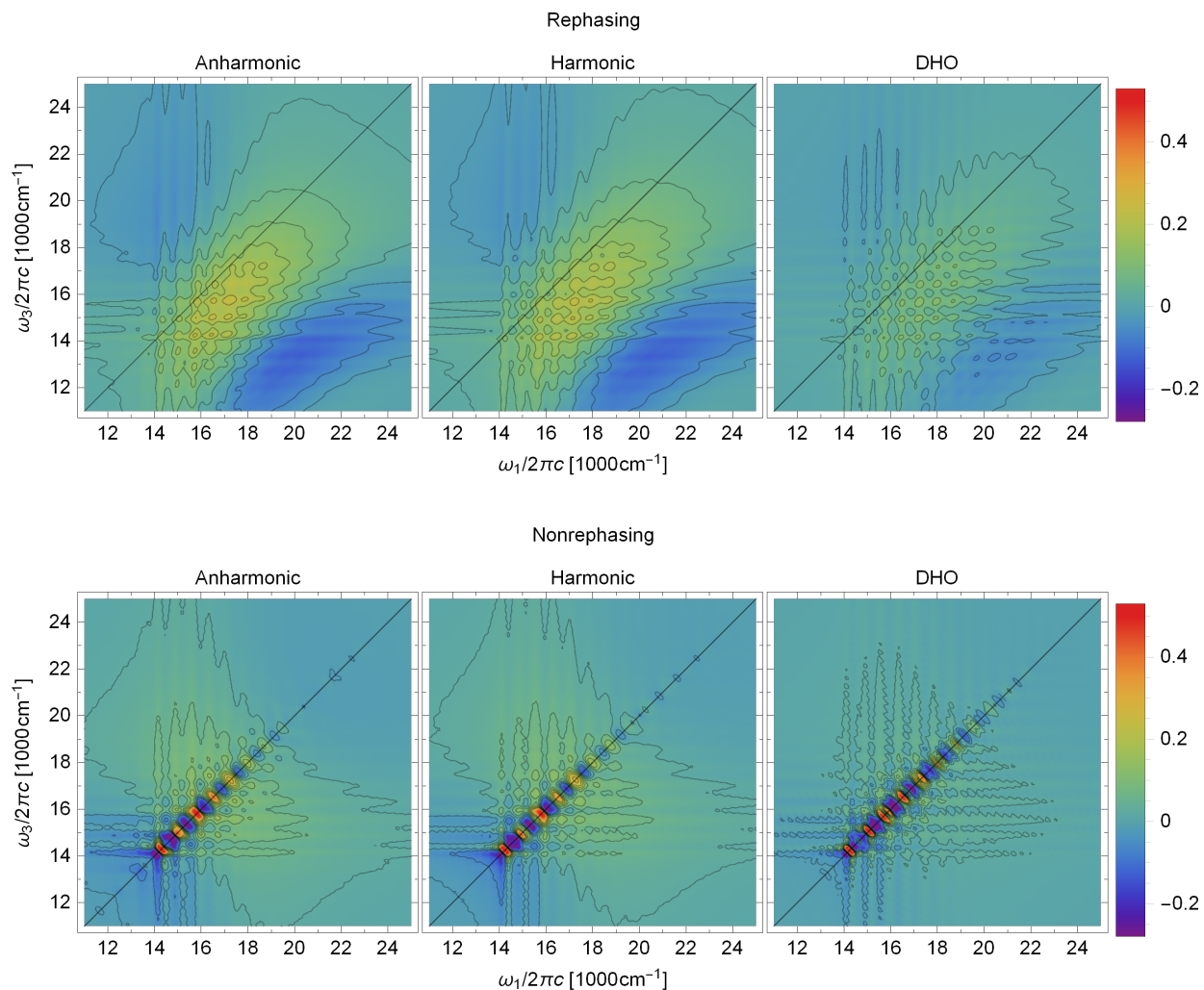


Figure S2: Rephasing (top) and nonrephasing (bottom) contributions to the two-dimensional spectra from Fig. 4 of the main text, computed with the on-the-fly ab initio single-Hessian thawed Gaussian approximation (“Anharmonic”, left), harmonic approximation (middle), and the displaced harmonic oscillator (DHO) model (right).

5 Two-dimensional spectra at $t_2 > 0$

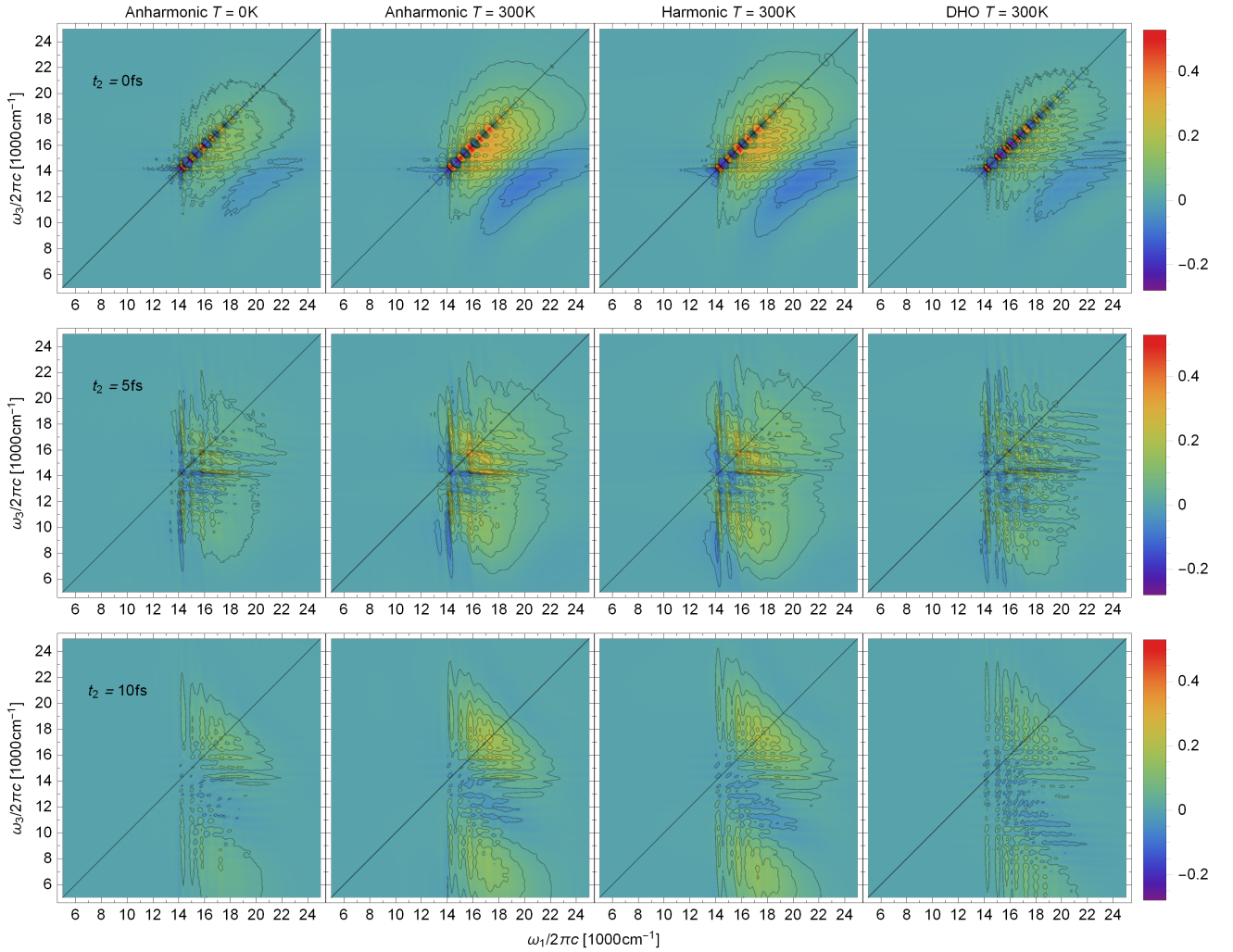


Figure S3: Two-dimensional electronic spectra [Eq. (3) of the main text] at delay times $t_2 = 0, 5, 10$ fs, computed with the on-the-fly ab initio single-Hessian thawed Gaussian approximation (“Anharmonic”) at 0 K (first column) and 300 K (second column), harmonic approximation at 300 K (third column), and the displaced harmonic oscillator (DHO) at 300 K model (fourth column). Each spectrum shows the sum of the ground-state bleach and stimulated emission terms [first two terms on the right-hand sides of Eqs. (6) and (7) of the main text] corresponding to the S_1 – S_0 electronic transition in azulene. At zero delay, the ground-state bleach and stimulated emission contributions are indistinguishable. However, already after 5 or 10 fs, the stimulated emission signal moves away from the diagonal, whereas the ground-state bleach spectrum remains close to the diagonal. At later t_2 delays (see Fig. S4), the stimulated emission starts returning towards the diagonal, reflecting coherent wavepacket dynamics in the excited electronic state. Indeed, the period of about 20–25 fs corresponds to the faster displaced modes (see Table S1). However, the recurrence is incomplete due to the slower dynamics in the other highly displaced modes.

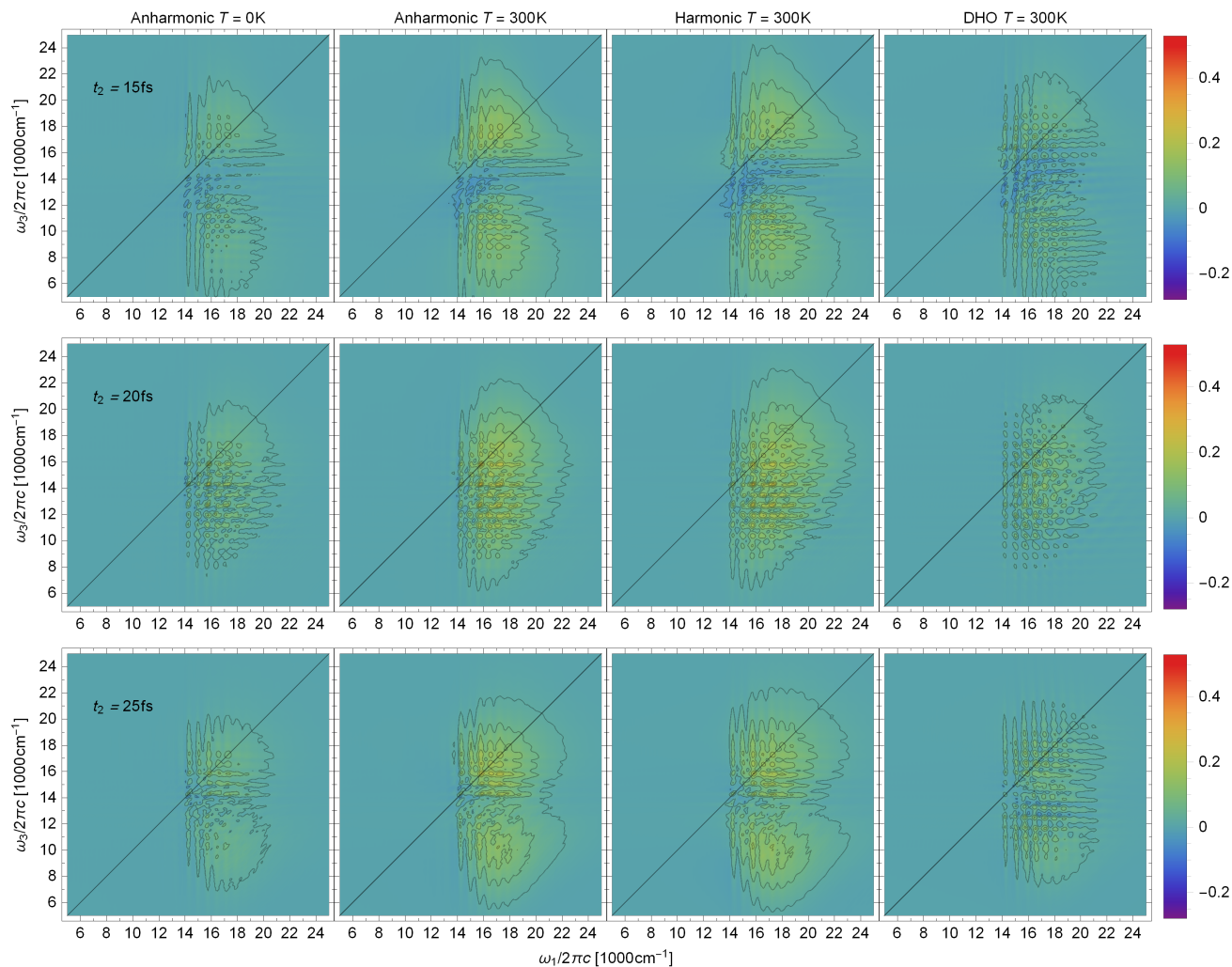


Figure S4: Same as Fig. S3 but for delay times $t_2 = 15, 20, 25$ fs.

Table S1: The most displaced modes of azulene. Ground-state frequencies ω_i of the normal modes are reported in terms of the wavenumber. The dimensionless displacements are defined as $\Delta_i = |\sqrt{\omega_i/\hbar}q_{2,i}|$, where q_2 is the excited-state minimum geometry expressed in the mass-scaled normal mode coordinates of the ground electronic state and $q_{2,i}$ is its component along mode i . Only the modes with $\Delta_i > 0.25$ are shown.

Wavenumber / cm^{-1}	Displacement
1660	0.92
1490	0.83
1425	1.22
1304	0.68
834	1.44
677	0.78
403	0.49

6 $|S_{\mathbf{R}}(t_3, 0, t_1)|$ at short t_1 and t_3 times

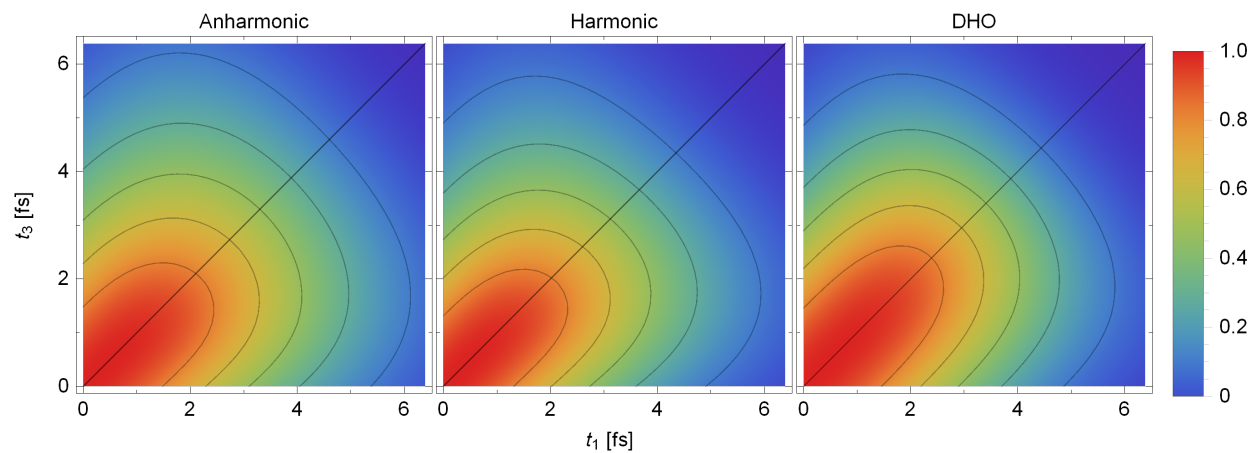


Figure S5: First 6 fs of $|S_{\mathbf{R}}(t_3, 0, t_1)|$ (see Fig. 4 of the main text) computed with the on-the-fly ab initio thawed Gaussian approximation (“Anharmonic”), harmonic approximation, and the displaced harmonic oscillator (DHO) model.

7 (A)symmetry of the rephasing and nonrephasing signals in the time domain

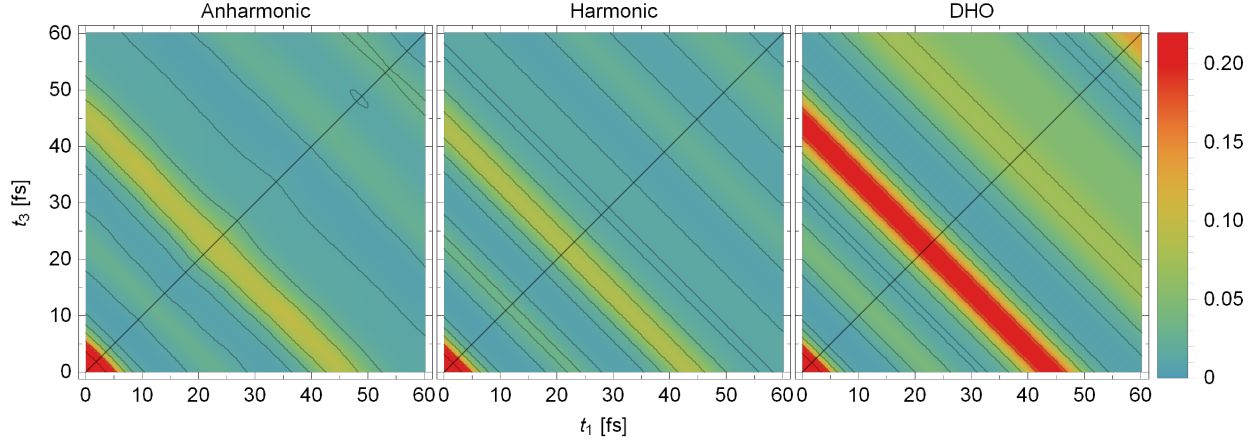


Figure S6: Absolute value of the nonrephasing time-domain signal ($|S_{\text{NR}}(t_3, 0, t_1)|$) at zero time delay ($t_2 = 0$), including only the ground-state bleach and stimulated emission terms [first two terms on the right-hand side of Eq. (7) of the main text], computed with the on-the-fly ab initio single-Hessian thawed Gaussian approximation (“Anharmonic”, left), harmonic approximation (middle), and the displaced harmonic oscillator (DHO) model (right) at 300 K.

In Fig. S6, we show that the absolute value of the nonrephasing signal $S_{\text{NR}}(t_3, 0, t_1)$ at $t_2 = 0$ is symmetric with respect to the diagonal $t_1 = t_3$ for all three—anharmonic, harmonic, and the displaced harmonic oscillator—models, whereas the rephasing signal $|S_{\text{R}}(t_3, 0, t_1)|$ (Fig. 4 of the main text) exhibits this symmetry only for the displaced harmonic oscillator model. Indeed, if we assume the Condon approximation ($\hat{\mu}_{21} \approx \mu = \text{const.}$) and include only the ground-state bleach and stimulated emission contributions, the nonrephasing signal at $t_2 = 0$ can be rewritten as a function of $t_1 + t_3$:

$$S_{\text{NR}}(t_3, 0, t_1) = C_1(0, t_3, t_1 + t_3) + C_1(-t_3, 0, t_1) \quad (23)$$

$$= 2|\mu|^4 \text{Tr}[\hat{\rho} e^{i\hat{H}_1(t_1+t_3)/\hbar} e^{-i\hat{H}_2(t_1+t_3)/\hbar}] \quad (24)$$

$$= S_{\text{NR}}(t_1, 0, t_3) \quad (25)$$

and is, therefore, symmetric with respect to the exchange of t_1 and t_3 . In going from (23) to (24), we used the definition of C_1 [Eq. (8) of the main text], the Condon approximation, the fact that $\hat{\rho}$ commutes with the ground-state vibrational Hamiltonian \hat{H}_1 , and the cyclic property of the trace. The same, however, does not hold for the rephasing contribution:

$$S_R(t_3, 0, t_1) = 2C_1(t_1, t_3, t_3) \quad (26)$$

$$= 2|\mu|^4 \text{Tr}[\hat{\rho} e^{i\hat{H}_2 t_1/\hbar} e^{i\hat{H}_1 t_3/\hbar} e^{-i\hat{H}_2 t_3/\hbar} e^{-i\hat{H}_1 t_1/\hbar}] \quad (27)$$

$$\neq 2|\mu|^4 \text{Tr}[\hat{\rho} e^{i\hat{H}_2 t_3/\hbar} e^{i\hat{H}_1 t_1/\hbar} e^{-i\hat{H}_2 t_1/\hbar} e^{-i\hat{H}_1 t_3/\hbar}] \quad (28)$$

$$= S_R(t_1, 0, t_3). \quad (29)$$

Yet, within the displaced harmonic oscillator model, the symmetry is recovered for the absolute value of $S_R(t_1, 0, t_3)$. This is discussed in the following Section.

8 Symmetry of the two-dimensional signal within the second-order cumulant approximation

Within the second-order cumulant method,^{S1} assuming only two electronic states (i.e., neglecting the excited-state absorption) and the Condon approximation ($\hat{\mu} \approx \mu = \text{const.}$), the components $R_\alpha(t_3, t_2, t_1)$ of the third-order response function (1) are approximated as

$$R_1(t_3, t_2, t_1) = |\mu|^4 e^{-i\omega_{21} t_1 - i\omega_{21} t_3} e^{-g(t_3)^* - g(t_1) - f_+(t_3, t_2, t_1)}, \quad (30)$$

$$R_2(t_3, t_2, t_1) = |\mu|^4 e^{i\omega_{21} t_1 - i\omega_{21} t_3} e^{-g(t_3)^* - g(t_1)^* + f_+(t_3, t_2, t_1)^*}, \quad (31)$$

$$R_3(t_3, t_2, t_1) = |\mu|^4 e^{i\omega_{21} t_1 - i\omega_{21} t_3} e^{-g(t_3) - g(t_1)^* + f_-(t_3, t_2, t_1)^*}, \quad (32)$$

$$R_4(t_3, t_2, t_1) = |\mu|^4 e^{-i\omega_{21} t_1 - i\omega_{21} t_3} e^{-g(t_3) - g(t_1) - f_-(t_3, t_2, t_1)}, \quad (33)$$

where

$$\omega_{21} = \frac{1}{\hbar} \text{Tr}[(\hat{V}_2 - \hat{V}_1)\hat{\rho}] \quad (34)$$

is the thermally averaged electronic energy gap, \hat{V}_i are the potential energy operators in the ground ($i = 1$) or excited ($i = 2$) electronic states,

$$g(t) = \frac{1}{\hbar^2} \int_0^t d\tau_2 \int_0^{\tau_2} d\tau_1 \text{Tr}[e^{i\hat{H}_1\tau_1/\hbar} \Delta\hat{V} e^{-i\hat{H}_1\tau_1/\hbar} \Delta\hat{V} \hat{\rho}], \quad (35)$$

$\Delta\hat{V} = \hat{V}_2 - \hat{V}_1 - \hbar\omega_{21}$, and

$$f_-(t_3, t_2, t_1) = g(t_2) - g(t_2 + t_3) - g(t_1 + t_2) + g(t_1 + t_2 + t_3), \quad (36)$$

$$f_+(t_3, t_2, t_1) = g(t_2)^* - g(t_2 + t_3)^* - g(t_1 + t_2) + g(t_1 + t_2 + t_3). \quad (37)$$

For simple systems, such as a pair of harmonic potentials, exact quantum-mechanical $g(t)$ can be found analytically.^{S1,S9} The second-order cumulant expansion is exact only in the special case of the displaced harmonic (Brownian) oscillator model. For general potentials, efficient classical approximations to $g(t)$ can be employed, at the price of introducing additional approximations in the evaluation of the response function (1). Remarkably, it is easy to show that, no matter how $g(t)$ is computed, the symmetry relationship

$$|R_\alpha(t_3, t_2, t_1)| = |R_\alpha(t_1, t_2, t_3)|, \quad \alpha = 1, \dots, 4, \quad (38)$$

holds for the four second-order cumulant expressions (30)–(33). For example, for R_3 we have

$$|R_3(t_3, t_2, t_1)|^2 = R_3(t_3, t_2, t_1)^* R_3(t_3, t_2, t_1) \quad (39)$$

$$= e^{-g(t_3)^* - g(t_1) + f_-(t_3, t_2, t_1)} e^{-g(t_3) - g(t_1)^* + f_-(t_3, t_2, t_1)^*} \quad (40)$$

$$= e^{-2\text{Re}[g(t_3) + g(t_1) - f_-(t_3, t_2, t_1)]} \quad (41)$$

$$= e^{-2\text{Re}[g(t_1) + g(t_3) - f_-(t_1, t_2, t_3)]} \quad (42)$$

$$= |R_3(t_1, t_2, t_3)|^2, \quad (43)$$

where (42) follows from (41) because

$$f_-(t_3, t_2, t_1) = f_-(t_1, t_2, t_3). \quad (44)$$

Similar procedure can be followed for other R_α functions, where we also need to use the relation:

$$\text{Re}f_+(t_3, t_2, t_1) = \text{Re}f_+(t_1, t_2, t_3). \quad (45)$$

Since the exact R_α for the displaced harmonic oscillator model can be written in the form of Eqs. (30)–(33), the proof holds in this special case as well.

Equation (38) implies that the symmetry with respect to exchanging t_1 and t_3 is present for arbitrary delay t_2 . However, in experiments, one cannot measure individual components of the response function but only their linear combination. For example, the signal measured in the rephasing phase-matching direction is^{S2}

$$S_R(t_3, t_2, t_1) = R_2(t_3, t_2, t_1) + R_3(t_3, t_2, t_1). \quad (46)$$

Then,

$$|S_R(t_3, t_2, t_1)|^2 = |R_2(t_3, t_2, t_1)|^2 + |R_3(t_3, t_2, t_1)|^2 + 2\text{Re}[R_3(t_3, t_2, t_1)^* R_2(t_3, t_2, t_1)] \quad (47)$$

$$\neq |S_R(t_1, t_2, t_3)|^2 \quad (48)$$

because

$$R_3(t_3, t_2, t_1)^* R_2(t_3, t_2, t_1) = e^{-g(t_3)^* - g(t_1) + f_-(t_3, t_2, t_1)} e^{-g(t_3)^* - g(t_1)^* + f_+(t_3, t_2, t_1)^*} \quad (49)$$

$$= e^{-2g(t_3)^* - 2\text{Re}[g(t_1)] + f_-(t_3, t_2, t_1) + f_+(t_3, t_2, t_1)^*} \quad (50)$$

$$= e^{-2g(t_3)^* - 2\text{Re}[g(t_1)] + 2g(t_2) - 2g(t_2 + t_3) - 2\text{Re}[g(t_1 + t_2)] + 2\text{Re}[g(t_1 + t_2 + t_3)]} \quad (51)$$

$$\neq e^{-2g(t_1)^* - 2\text{Re}[g(t_3)] + 2g(t_2) - 2g(t_1 + t_2) - 2\text{Re}[g(t_2 + t_3)] + 2\text{Re}[g(t_1 + t_2 + t_3)]} \quad (52)$$

$$= e^{-2g(t_1)^* - 2\text{Re}[g(t_3)] + f_-(t_1, t_2, t_3) + f_+(t_1, t_2, t_3)^*} \quad (53)$$

$$= R_3(t_1, t_2, t_3)^* R_2(t_1, t_2, t_3). \quad (54)$$

Nevertheless, the equality is restored at $t_2 = 0$ because $R_2(t_3, 0, t_1) = R_3(t_3, 0, t_1)$:

$$|S_R(t_3, 0, t_1)|^2 = 4|R_3(t_3, 0, t_1)|^2 = 4|R_3(t_1, 0, t_3)|^2 = |S_R(t_1, 0, t_3)|^2. \quad (55)$$

References

- (S1) Mukamel, S. *Principles of nonlinear optical spectroscopy*, 1st ed.; Oxford University Press: New York, 1999.
- (S2) Schlau-Cohen, G. S.; Ishizaki, A.; Fleming, G. R. Two-dimensional electronic spectroscopy and photosynthesis: Fundamentals and applications to photosynthetic light-harvesting. *Chem. Phys.* **2011**, *386*, 1–22.
- (S3) Suzuki, M. Thermo Field Dynamics in Equilibrium and Non-Equilibrium Interacting Quantum Systems. *J. Phys. Soc. Jap.* **1985**, *54*, 4483–4485.
- (S4) Borrego-Varillas, R.; Nenov, A.; Ganzer, L.; Oriana, A.; Manzoni, C.; Tolomelli, A.; Rivalta, I.; Mukamel, S.; Garavelli, M.; Cerullo, G. Two-dimensional UV spectroscopy: A new insight into the structure and dynamics of biomolecules. *Chem. Sci.* **2019**, *10*, 9907–9921.

- (S5) Picchiotti, A.; Nenov, A.; Giussani, A.; Prokhorenko, V. I.; Miller, R. J. D.; Mukamel, S.; Garavelli, M. Pyrene, a Test Case for Deep-Ultraviolet Molecular Photo-physics. *J. Phys. Chem. Lett.* **2019**, *10*, 3481–3487.
- (S6) Begušić, T.; Vaníček, J. On-the-fly ab initio semiclassical evaluation of third-order response functions for two-dimensional electronic spectroscopy. *J. Chem. Phys.* **2020**, *153*, 184110.
- (S7) Khalil, M.; Demirdöven, N.; Tokmakoff, A. Obtaining absorptive line shapes in two-dimensional infrared vibrational correlation spectra. *Phys. Rev. Lett.* **2003**, *90*, 4.
- (S8) Anda, A.; Abramavičius, D.; Hansen, T. Two-dimensional electronic spectroscopy of anharmonic molecular potentials. *Phys. Chem. Chem. Phys.* **2018**, *20*, 1642–1652.
- (S9) Zuehlsdorff, T. J.; Hong, H.; Shi, L.; Isborn, C. M. Nonlinear spectroscopy in the condensed phase: The role of Duschinsky rotations and third order cumulant contributions. *J. Chem. Phys.* **2020**, *153*, 044127.